APC-mutant cells exploit compensatory chromosome alterations to restore tumour cell fitness

Yoshihiro Kawasaki[1,2], Tomoko Hamaji[1], Koji Owada[1], Akiko Hayashi[1], Yuping Wu[1], Taisaku Nogi[1], Miwa Okada[1,†], Shoko Sakai[1], Naoko Tokushige[1], Yuta Kouyama[3], Atsushi Niida[4], Koshi Mimori[3], Toshihiko Kuroda[5], Takao Senda[6], Miho Ohsugi[7], Katsumi Fumoto[8], Akira Kikuchi[8], Per O. Widlund[9], Kazuyuki Kiyosue[10], Norio Yamashita[11], Masahiko Morita[11], Hideo Yokota[11], Satya N. V. Arjunan[12], Wei-Xiang Chew[12,13], Koichi Takahashi[12], Wesley R. Legant[14,††], Bi-Chang Chen[14,†††], Eric Betzig[14,††††], Ron Smits[15], Riccardo Fodde[16], Hiroko Oshima[17], Masanobu Oshima[17], M. Mark Taketo[18], Tetsu Akiyama[2], Yuko Mimori-Kiyosue[1,*]

[1]Laboratory for Molecular and Cellular Dynamics, RIKEN Center for Biosystems Dynamics Research, Kobe 650-0047, Japan

[2]Laboratory of Molecular and Genetic Information, Institute of Molecular and Cellular Biosciences, The University of Tokyo, Tokyo 113-0032, Japan

[3]Department of Surgery, Kyushu University Beppu Hospital, Beppu 874-0838, Japan

[4]Division of Health Medical Computational Science, Health Intelligence Center, Institute of Medical Science, The University of Tokyo, Tokyo 108-8639, Japan

[5]Nico-tama Coloproctology Clinic, Tokyo 158-0094, Japan

[6]Department of Anatomy, Graduate School of Medicine, Gifu University, Gifu 501-1194, Japan

[7]Department of Life Sciences, Graduate School of Arts and Sciences, The University of Tokyo, Tokyo 153-8902, Japan

[8]Department of Molecular Biology and Biochemistry, Graduate School of Medicine, Osaka University, Osaka 565-0871, Japan

[9]Department of Microbiology and Immunology, University of Gothenburg, Gothenburg 405 30, Sweden

[10]Biomedical Research Institute, National Institute of Advanced Industrial Science and Technology, Ikeda 563-0026, Japan

[11]Image Processing Research Team, Center for Advanced Photonics, RIKEN, Saitama 351-0198, Japan

[12]Laboratory for Biologically Inspired Computing, RIKEN Center for Biosystems Dynamics Research, Osaka 565-0874, Japan

[13]Department of Physics, Faculty of Science, University of Malaya, 50603 Kuala Lumpur, Malaysia

[14]Janelia Research Campus, Howard Hughes Medical Institute, Ashburn, VA 20147, USA

[15]Department of Gastroenterology and Hepatology, Erasmus MC-University Medical Center, 3015 CE Rotterdam, The Netherlands

[16]Department of Pathology, Erasmus MC Cancer Institute, Erasmus University Medical Center, 3000 CA Rotterdam, The Netherlands

[17]Division of Genetics, Cancer Research Institute, Kanazawa University, Ishikawa 920-1164, Japan

[18]Colon Cancer Project, Kyoto University Hospital-iACT, Graduate School of Medicine, Kyoto University, Yoshida-Honmachi, Sakyo, Kyoto 606-8501, Japan

[†]Present address: Department of Immunology, Laboratory of Immunology, Institute of Biomedical Research and Innovation (IBRI), 6-3-7,Minatojima-minamimachi, Chuo-ku, Kobe 650-0047 Japan

[††]Present address: Joint Department of Biomedical Engineering, UNC, Chapel Hill, NC 27599, USA, and NCSU Raleigh, NC 27695, USA; Department of Pharmacology, University of North Carolina, Chapel Hill, NC, USA

[†††]Present address: Research Center for Applied Sciences, Academia Sinica, Taipei 115-29, Taiwan

[††††]Present address: Departments of Physics and Molecular and Cell Biology, University of California, Berkeley, CA 94720, USA; Howard Hughes Medical Institute, Berkeley, CA 94720, USA

*Correspondence to: Yuko Mimori-Kiyosue, Ph.D., Laboratory for Molecular and Cellular Dynamics, RIKEN Center for Biosystems Dynamics Research, 2-2-3 Minatojima-minamimachi, Chuo-ku, Kobe 650-0047, Japan

Tel.: +81-78-306-3070

Fax: +81-78-306-3118

E-mail: yuko.kiyosue@riken.jp

Abstract

Certain copy number alterations (CNAs) are strongly associated with particular cancer types. However, the mechanisms that underlie selection of specific CNAs remain unknown. Here, we identified functional relationships between recurrent CNAs in colorectal cancers (CRCs) and *adenomatous polyposis coli* (*APC*) mutations. Quantitative phenotyping of mitotic spindles highlighted APC functions at centrosomes where APC positively regulated Aurora A kinase (AURKA). Upon APC inactivation, elevated β-catenin levels blocked AURKA activation, which caused chromosome instability and suppressed proliferation, resulting in the generation and selection of AURKA-activating CNAs. Arm-level amplification of chromosomes that contained AURKA and AURKA activator genes was observed in *APC*-mutant CRCs, early stage mouse tumours, and cells in culture, which was concomitant with an increase in growth potential. Our findings demonstrate a mechanism that restores tumour cell fitness through compensatory chromosome alterations to overcome adverse effects of prior mutations, which may affect the course of cancer type-specific CNA formation.

Introduction

A chromosome number abnormality is one of the most common characteristics of cancer. Recent advances in genome characterization technologies have revealed the genomic landscape of cancer and identified recurrent copy number alterations (CNAs) that include arm-level and focal CNAs[1, 2]. The strong association of certain CNAs with particular cancer types and lineages[1, 3] raises questions regarding the mechanisms that underlie the selection of cancer type-specific CNAs and their functional consequences. Additionally, a paradox has emerged: because arm-level CNAs, which have been referred to as segmental or partial aneuploidies[4], in normal cells exert negative effects on cellular and organismal fitness and growth by disrupting cellular homeostasis[4, 5], it is unclear how cancer cells can have such a mutational burden.

CNAs are generated by various mechanisms[6, 7]. The major causes of arm-level CNAs are defects in chromosome segregation[6], whereas mechanisms that involve double-strand break repair and DNA replication have been proposed for more complicated or focal CNAs[7]. Recent studies have shown that massive chromosome rearrangements, such as interchromosomal translocations and chromothripsis, occur in micronuclei, which are generated by chromosome mis-segregation during mitosis through a combination of mechanisms that include replication errors[7, 8, 9, 10]. However, it is largely unknown whether the mechanism of recurrent, cancer type-specific CNAs is due to structural or functional factors.

Tumour suppressor protein adenomatous polyposis coli (APC) as a component of the APC/AXIN/Glycogen synthase kinase (GSK) 3β complex (β-catenin destruction complex) has a well-established function in the WNT/β-catenin pathway. Specifically, it controls β-catenin levels[11, 12, 13]. APC is also associated with microtubule cytoskeletons and its dysfunction induces chromosome instability (CIN) (Extended Data Fig. 1)[14, 15, 16, 17]. Chromosome mis-segregation

because of premature mitotic exit is commonly observed after APC inactivation in various cell lines and mouse ES cells[16, 17, 18, 19]. Nevertheless, the mechanisms that underlie this CIN remain controversial[20]. Moreover, it remains unclear whether and how initiation of CIN by *APC* mutations drives tumour progression.

Mutations in the *APC* gene promote tumourigenesis through constitutive activation of the Wnt/β-catenin signalling pathway[21, 22, 23]. In the conventional model, Wnt signalling is activated immediately after homozygous loss of *APC*, which induces upregulation and nuclear accumulation of β-catenin that is required to evoke Wnt signalling and the proliferative response[11, 12, 13]. However, several studies have not been able to confirm nuclear accumulation of β-catenin in early lesions after *APC* loss, despite robust staining in later lesions of human adenomas and animal models[24, 25, 26], which raises the possibility of unexplained mechanisms for adenoma formation independent of Wnt/β-catenin signalling at early stages[27, 28].

Here, we determined the functional relationship between APC deficiency and *APC*-mutant tumour-specific CNAs through comparative analyses of APC functions in cultured cells and tumours. First, we identified the critical molecular mechanisms that involved Aurora A kinase (AURKA) and β-catenin, which induced CIN and growth retardation in *APC*-mutant cells. Next, we revealed the mechanisms that overcame the adverse effects of *APC* mutation by forming recurrent CNAs to improve the proliferation potential. Our findings demonstrated that *APC* mutant cells exploited their own CIN ability to acquire compensatory chromosome alterations required to restore cellular fitness, which provide a new insight into the mechanisms for the formation of cancer type-specific CNAs.

Results

Identification of an important phenotypic feature of mitotic spindles upon APC deficiency

Numerous studies have reported that APC cooperates with many mitotic regulators, which include spindle assembly checkpoint protein Bub1/R1 and microtubule-binding protein End-binding 1 (EB1), to ensure accurate chromosome separation[16, 17, 18, 29] (Extended Data Fig. 1). Notably, depletion of APC does not significantly affect spindle formation, but leads to chromosome mis-segregation[18, 30]. Despite accumulating knowledge regarding the molecular interactions, most essential mitotic functions of APC, which contribute to tumour progression over the long term, remain undetermined[20].

To quantitatively and precisely determine the overall spindle phenotype affected by APC deficiency, we employed lattice light sheet microscopy[31, 32] that enables high spatiotemporal resolution 3D live cell measurement of whole cells. Using this technique, we monitored microtubule growth dynamics by visualising GFP-fused End-binding 1 (EB1-GFP), a marker of newly assembled microtubule ends[33] (Fig. 1a, Extended Data Fig. 2, and Movie 1–3). To detect even slight differences, we integrated numerous time point images from multiple cells *in silico* and found that the microtubule growth probability was reduced significantly around centrosomes after APC depletion (Fig. 1b, c). This result indicated that the centrosomes were immature under APC deficiency.

Consistent with this finding, accumulation of γ-tubulin at centrosomes and activation of centrosomal kinases AURKA (autophosphorylation at T288) and polo-like kinase 1 (PLK1; phosphorylation at T210), which are central mitotic kinases that cooperatively regulate

centrosome maturation[34, 35], were reduced significantly in APC-depleted cells (Fig. 2a; Extended Data Table 1).

APC regulates AURKA activity together with AXIN1 and β-catenin

To determine the molecular mechanism of centrosome regulation by APC, we screened centrosomal proteins involved in centrosome maturation for their association with APC. We found that APC bound to AURKA, PCNT (pericentrin), and ch-TOG through its N- and/or C-terminal regions (Fig. 2b, Extended Data Fig. 3, and Extended Data Table 2). Among these interactors, AURKA has been reported to act upstream of the others to regulate centrosome maturation[34, 35, 36]. Therefore, we further investigated APC functions in AURKA regulation.

We did not detect promotion of AURKA activation by APC *in vitro*. Because AURKA interacts with AXIN1, a core scaffold in the β-catenin destruction complex with APC[11], and disrupts the complex to stabilize β-catenin[37] (Extended Data Fig. 4a), we investigated the effect of AXIN1 and β-catenin on AURKA activation. We found that the middle portion of AXIN1 promoted AURKA activation by *in vitro* assays and in HEK293T cells, which was similar to TPX2, a well-characterized activator of AURKA[38] (Fig. 2c, d and Extended Data Fig. 4b). Strikingly, elevated β-catenin levels inhibited AXIN1-mediated AURKA activation (Fig. 2e). The N-terminal region of APC facilitated AXIN1-mediated AURKA activation significantly (Fig. 2f). Because expression of a longer APC fragment that lacked only the C-terminal region was technically difficult, we used MEFs from *Apc*^{1638T} mice without the C-terminal half of APC[39] and confirmed that the C-terminal region of APC activated AURKA (Extended Data Figs. 1b and 4c, d). Taken together, APC positively regulates AURKA activity via two mechanisms:

promoting AXIN1-mediated AURKA activation and β-catenin degradation, whereas APC inactivation inhibits AURKA activation indirectly through increased levels of β-catenin.

Elevated β-catenin levels block AURKA activation at centrosomes

In tumours and cancers, *APC* is genetically truncated or lost[21, 22, 40, 41] (Extended Data Fig. 1). To investigate cooperation of APC with AURKA under conditions similar to the disease, we used the non-cancerous p53-proficient human mammary epithelial cell line MCF10A and the MCF10A-derived cell line APC883 that harbours a homozygous *APC* truncation (Extended Data Fig. 1b). Consistent with previous reports[16, 17, 18], chromosome separation errors monitored by the appearance of lagging chromosomes were increased significantly in APC883 cells (Fig. 3a), which were associated with chromosomal defects (Extended Data Fig. 5a, b and Extended Data Table 3). In these cells, β-catenin levels were elevated and the activated fraction of AURKA at the centrosomes was reduced as expected, although total AURKA levels were increased (Fig. 3a and Extended Data Fig. 2c). When β-catenin levels were reduced to the same levels as those in parental cells by RNA interference (Extended Data Fig. 2c), AURKA activity was restored and the frequency of chromosome separation errors was reduced by ~20%, although the error frequency was still significantly higher than that in parental cells (Fig. 3a, Extended Data Fig. 5c). Introduction of the constitutively active form of AURKA, AURKA (T288D) also partially reduced chromosome separation errors, while the error reduction was even weaker with the introduction of AURKA activator TPX2 (Fig. 3a, Extended Data Fig. 5d, e). Additionally, it has been reported that ES cells from *Apc*^{1638T} mice display a weak CIN phenotype, while β-catenin is not upregulated in these mice[16, 39] (Extended Data Fig. 1b). These results indicated that

stabilization of β-catenin was the major cause of CIN by inhibiting AURKA activation even in the presence of truncated APC, but full-length APC still suppressed CIN.

As an underlying mechanism of AURKA inhibition by β-catenin, we found that stabilized β-catenin perturbed the dynamics of AURKA at centrosomes. Localization of AXIN1 and β-catenin to centrosomes and their involvement in mitotic centrosome functioning have been reported[42, 43, 44, 45]. Exogenous expression of a dominant stable form of β-catenin (MMβ-catenin), in which the GSK phosphorylation sites that promote destruction have multiple mutations[11], in parental MCF10A cells resulted in accumulation of AURKA on spindles along with MMβ-catenin, while the fraction of active AURKA was decreased (Fig. 3b and Extended Data Fig. 2d). Fluorescence recovery after photobleaching (FRAP) analysis to monitor the mobility of molecules revealed that turnover of GFP-AURKA at centrosomes was delayed in MMβ-catenin-expressing cells compared with cells transfected with wildtype β-catenin (Fig. 3c and Extended Data Fig. 2e). These results suggested that stabilized β-catenin sequestered AURKA in non-functional complexes on spindles.

Strikingly, analysis of mitosis duration showed that it was unchanged in APC883 cells, which indicates the lack of a checkpoint function (Fig. 3d). Expression of active AURKA(T288D) in APC883 cells prolonged the mitosis duration concomitant with a reduction in chromosome separation errors, which suggests a checkpoint response. However, expression of TPX2 in APC883 cells did not increase the mitosis duration. These results indicated that forced activation of AURKA by activating factors such as TPX2 in the presence of excess β-catenin and the absence of functional APC did not restore mitotic fidelity. Consistently, it was reported that TPX2 overexpression in hTERT RPE-1 cells (an immortalized retinal pigment epithelial cell line) induces significant defects in mitotic spindle assembly and progression through mitosis[46].

These all observations indicated that *APC* mutation led to AURKA dysregulation and impaired spindle checkpoint function (model in Fig. 3e).

Upregulation of AURKA in *APC*-mutant tumours

To evaluate our models, we investigated the state of AURKA activation in *APC*-mutant tumours using $Apc^{\Delta 716}$ mice with a heterozygous *Apc* truncation mutation that leads to severe polyposis after loss of the wildtype allele[47] (Extended Data Fig. 1). Analysis of multiple polyps in comparison with crypts showed that AURKA activity as a ratio of phosphorylated to total AURKA staining was unexpectedly higher in many polyps than in crypts, while β-catenin staining was increased in tumour cells (Fig. 4a, b and Extended Data Fig. 6a, b). The staining intensity of TPX2 also showed an increasing trend (Extended Data Fig. 6c). Consistently, in human *APC*-mutant early-stage tumours, increases of AURKA activity and TPX2 levels were observed concomitantly with increased proliferative activity (Fig. 4c and Extended Data Fig. 7). Considering the nature of *APC*-mutant cells with the CIN phenotype, these changes were considered to be induced by genetic alteration. If so, AURKA-activated cells appeared because of gaining AURKA-activating genes.

Upregulation of AURKA in *APC*-mutant cancers and clinical manifestations

This assumption was in accordance with the observation that, among the recurrent increases and decreases in many of the chromosomes, the long arm of chromosome 20 (20q), which carries *AURKA* and *TPX2* genes located on 20q at 20q13.2 and 20q11, respectively, is frequently amplified in human colorectal cancers (CRCs)[2]. It is also noteworthy that chromosome 13q, the

second most frequently amplified chromosome in CRCs[2], contains *BORA* at 13q21.33, which encodes another AURKA-activating factor[48]. Because the association of *APC* mutations with amplification of these loci had not been investigated, we reanalysed The Cancer Genome Atlas (TCGA) dataset[2] for *APC* mutations. The results demonstrated that amplifications of 20q and 13q were significantly more frequent in cancers with *APC* mutations than in those without them (Fig. 5a) and APC-mutant cancers had significantly higher copy numbers of these chromosome arms (Fig. 5b). Although amplifications of 20q and 13q are relatively high even in cancers without an *APC* mutation, it is possible that this fraction has Wnt pathway activity modulated by mutations in AXIN or GSK3β, or by dysregulation of Wnt secretion[49].

The rate of *APC* mutation was higher in the microsatellite stable (MSS) subtype (the majority of MSS CRCs demonstrate CIN) than in the microsatellite instable (MSI) subtype (Fig. 5c). Also in the consensus molecular subtype (CMS) classification, *APC* mutations have been shown to be significantly enriched in CMSs with somatic copy number alterations[50], which is consistent with the notion that *APC* mutation contributes to the development of tumours with CNAs. Furthermore, there was a significant statistical association between 20q/13q amplification and metastasis that included lymphatic and distant metastases (Fig. 5d), which is often associated with reduced survival[51, 52]. It has also been reported that high expression of AURKA in colorectal cancer and liver metastasis of colorectal cancer is associated with a poor prognosis[53, 54].

AURKA-activating CNAs at the early stage of tumourigenesis

We next investigated whether AURKA-activating CNAs are initiated at the early stage of tumourigenesis using the *Apc*$^{\Delta 716}$ mouse. We performed high resolution array-based comparative

genomic hybridization (aCGH) analysis to detect DNA copy number alterations in individual polyps from *Apc*$^{\Delta 716}$ mice. In the mouse genome, *Aurka*/*Tpx2* and *Bora* loci reside on chromosomes 2 H3/2 H1 and 14 E2.2, respectively (Fig. 5e). The three examined polyps all exhibited amplification of *Tpx2*, amplification of the *Aurka* and *Bora* loci was found in two polyps (Fig. 5e). Syntenic comparison of human and mouse chromosomes showed cross-species overlaps in the amplified regions, which suggested that these *AURKA*-related loci were selected by functional relevance rather than structural factors. Furthermore, we analysed relative DNA content of *Aurka*, *Tp*x2, and *Bora* in multiple polyps from *Apc*$^{\Delta 716}$ mice and in human polyp #2 diagnosed as a benign tumour (Fig. 5f). These genes are frequently increased in such polyps.

To confirm the occurrence of chromosome mis-segregations in *Apc*$^{\Delta 716}$ mouse tumours, we counted micronuclei positive for phosphorylated histone H2A.X (γH2A.X) that accumulates at high levels in damaged DNA, which is often generated in mis-segregated and damaged chromosomes[8, 55]. In *Apc*$^{\Delta 716}$ mice, the incidence of γH2A.X-positive micronuclei was higher in the intestinal tumours than in crypts with normal morphology (Fig. 6a).

In *Apc*$^{\Delta 716}$ mouse polyps and human polyp #2, we found localized areas with intense AURKA immunostaining even in the interphase cells (Fig. 6b). Because normal AURKA expression is limited during mitosis, AURKA expression was dysregulated in these areas. These observations demonstrated that AURKA-overexpressing cells had appeared within tumour tissues at the early stage of tumourigenesis.

AURKA-activating CNAs promote cell proliferation

Next, we investigated why AURKA-activated CNAs were selected. Direct visualization of the cell division cycle by live imaging revealed that the doubling time of APC883 cells was about twice as long as that of parental MCF10A cells (Fig. 7a, b and Movies 4–6). Strikingly, a reduction of the β-catenin level in APC883 cells, which recovered AURKA activity (Fig. 3a), dramatically restored the doubling time to the same as that of parental MCF10A cells (Fig. 7a, b). Introduction of active AURKA (T288D) or TPX2 recovered the doubling time as expected, albeit partially. These results indicated that blockade of AURKA activation by stabilized β-catenin was the major cause of the delay in the cell cycle and thus additional AURKA activation was required to proliferate. Notably, expression of dominant stable MMβ-catenin in MCF10A cells did not delay the doubling time (Fig. 7b). In these cells, active AURKA levels were maintained similarly to those in control cells owing to the increase of total AURKA levels (Fig. 3b). Therefore, full-length APC cancelled the adverse effects of stabilized β-catenin on cell proliferation. In these cells, phosphorylated AURKA levels were maintained at levels comparable to control cells. (Fig 3b).

As the passage number increased, a subgroup of APC883 cells with a higher growth rate appeared spontaneously and became dominant in the culture ("transformed APC883", Fig. 7b and Movie 5). These cells had acquired new abnormal karyotypes that consisted of a near tetraploid chromosome content including common numerical imbalances (Fig. 7c and Extended Data Fig. 5f). Remarkably, chromosome 20 was the most abundant at six copies per cell. In these cells, active AURKA was restored to levels comparable to those in parental MCF10A cells because of the increase in total AURKA levels (Fig. 7d).

To confirm the contribution of chromosome 20 to proliferation rate regulation, we isolated MCF10A subclones with chromosome 20 disomy [MCF10A(20di)] or trisomy

[MCF10A(20tri)] (Extended Data Fig. 5a, Type No. 2 and Type No. 1, respectively; see also Extended Data Table 3). Doubling time of MCF10A(20tri) cells was significantly longer than that of MCF10A(20di) cells (Fig. 7e). Strikingly, APC depletion in MCF10A(20tri) cells shortened the doubling time, whereas APC depletion in MCF10A(20di) cells prolonged doubling time as expected (Fig. 7e, Extended Data Fig. 2f and Movie 7). In MCF10A(20tri) cells, both t-AURKA and phosphorylated AURKA levels were higher than in MCF10A(20di) cells, whereas after APC depletion, phosphorylated AURKA levels were reduced to a level comparable to that in APC-depleted MCF10A(20di) cells. These results suggested that chromosome 20 amplification was advantageous for proliferation when APC activity was reduced.

Delayed cell cycle progression in *APC*-mutant cells

Our results indicated that increased levels of β-catenin suppressed cell cycle progression in *APC*-mutant cells. However, this notion appears to be inconsistent with the conventional understanding that tumour cells exhibit uncontrolled (fast) growth. Nevertheless, it has not been determined whether abnormal control of *APC*-mutant cell proliferation leads to an accelerated cell cycle.

Therefore, we estimated the cell cycle rate by measuring the ratio of dividing cells in mouse intestines. As shown in Fig. 7g, the proportion of dividing cells was significantly higher in crypts than in tumours, which suggested that these cells had a slower cell cycle rate than crypt cells that were undergoing normally controlled proliferation. Because the mitosis duration of APC883 cells was not prolonged (Fig. 3d), it was not a factor in the interpretation.

In the mouse and human tumours used in this study, increased β-catenin signals were observed throughout the cytoplasm without obvious nuclear accumulation (Extended Data Figs. 6b and 7c), which indicated that these cells were in this state before intense activation of Wnt signalling. This observation was consistent with their slow growth rate.

AURKA inhibition slows tumour cell growth

In *Apc*$^{\Delta 716}$ mice treated with AURKA inhibitors alisertib (MLN8237) or MLN8054, the abundance of cells positive for Ki67, a proliferation marker, was reduced among tumour cells, but remained unchanged in crypts (Fig. 8a, b). These results indicated that the tumour cells were more dependent on AURKA activity. Analysis of the polyp number showed that administration of the AURKA inhibitors particularly reduced the number of large polyps, which indicated that AURKA inhibition slowed tumour cell growth, although significant tumour regression was not observed (Fig. 8c, d). Additionally, when AURKA, TPX2, or BORA was depleted in CRC cell lines SW480 and HT29, which carried a truncated *APC* mutation, growth of these cells was suppressed (Fig. 8e, f, Extended Data Fig. 2g).

Taken together, our results demonstrated that, upon *APC* mutation, the induced CIN property allowed chromosome alteration and AURKA-activating CNAs were selected to evade the adverse effects of stabilized β-catenin, which was the first selection pressure in the formation of *APC*-mutant CRC-specific CNAs and affected the fate of tumour cells for a long period of time (Fig. 9).

Discussion

In this study, we performed comparative analyses of APC functions in cultured cells and mouse/human tumours, and identified two critical molecular mechanisms that are important to shape the cancer genome. One is the mechanism of CIN induced by APC deficiency. APC positively regulates AURKA activity in the normal state. Upon APC dysfunction, stabilized β-catenin blocks AURKA activation, which impairs centrosome maturation and causes chromosome mis-segregation. The other is the mechanism of recurrent CNA formation generated in *APC*-mutant tumours. AURKA blockade by stabilized β-catenin in *APC*-mutant cells causes a proliferation delay that results in the selection of compensatory CNAs that activate AURKA.

APC cooperates with AURKA in a complex with AXIN1 and β-catenin

We identified AURKA as a major dysregulated factor in *APC*-mutant cells at centrosomes by quantitative 3D mapping of spindle microtubule dynamics using lattice light sheet microscopy and computational analyses. In APC-deficient cells, the activated fraction of AURKA was reduced, which resulted in chromosome mis-segregation and a delayed cell cycle. APC activates AURKA together with Axin1, whereas APC deficiency increases the levels of β-catenin and blocks AURKA activation. Thus, APC acts as a scaffold for AURKA activation with AXIN1, which resembles the β-catenin destruction machinery[11], to regulate mitosis and cell cycle progression. However, in our experiments using MCF10A cells, restoration of the mitotic fidelity and proliferation rate of APC883 cells by introduction of active AURKA was partial. Because *APC* mutation or depletion causes CIN through β-catenin/TCF-mediated transcription[56, 57], it is possible that transcription-mediated CIN coexists in these cells.

Notably, the phenotype caused by AURKA inhibition in *APC*-mutant cells, which induced CIN without mitotic arrest, is unique because AURKA inhibition by genetic deletion or an inhibitory agent commonly leads to abnormal spindle formation and CIN followed by DNA damage-induced cell cycle arrest[35, 58]. The mechanisms of spindle checkpoint loss in *APC*-mutant cells should be further clarified in future studies.

APC functions in cell proliferation

Our results demonstrated that increased levels of β-catenin in *APC*-mutant cells had slowed cell cycle progression. This appears to conflict with the traditional model in which activation of Wnt/β-catenin signalling is the initiating event that underlies colon adenoma formation after loss of *APC*[59, 60, 61, 62]. However, our observations are in good agreement with another hypothesis in which the proliferative response of β-catenin in *APC*-mutant cells requires additional mutations, such as those in *KRAS*[28, 63], at later stages, because examinations of human early adenomas, intestinal polyps from *Apc* mutant rat models, and intestines from *apc* mutant zebrafish embryos have not confirmed the presence of nuclear β-catenin[24, 25, 26, 28]. All of these observations suggest that *APC* loss and upregulation of β-catenin can also be considered as independent causes of tumour initiation[28].

Importantly, exogenous expression of stable mutant β-catenin in the presence of full-length APC did not exert a disadvantageous effect on cellular proliferation, which suggested that APC cancels the unfavourable effects caused by increased levels of β-catenin. This is reasonable because Wnt/β-catenin signalling in normal developmental processes must not suppress cell proliferation.

Although in this study we showed a direct association between APC and AURKA at the protein level as well as their indirect association at the chromosomal level, *AURKA* amplification have been also reported in various cancer types, which demonstrates the major role of AURKA in tumour growth. Because aberrant Wnt signalling has been observed in many more cancer types[49], a decrease in AURKA activity due to stabilization of β-catenin may occur also in cancer types other than colorectal cancer.

CNAs in tumours

We confirmed an increase in the frequency of CIN and CNAs in mouse tumours. The fact that the region with the same gene was amplified in mice and humans, despite different chromosomal structures, strongly suggests that it occurred because of necessity. Comparison of syntenic regions and their CNAs may provide important clues for the mechanism of tumour development regulated at the chromosome level.

On the other hand, when considering CNA formation in different species, it is unlikely that the CNA formation processes are the same in humans and mice by considering the differences in human and mouse chromosomal structures. This may cause differences in the tumour phenotype and carcinogenicity as well as the efficacy of anti-cancer drugs in humans and mice. Because CIN is a major hallmark of cancer[64, 65], species dependence of the chromosome structure should be considered in cancer research and drug development.

The perspective of cancer treatment

Our observations in this study demonstrated that the growth of *APC*-mutant cells is sensitive to decreased AURKA activity. Because AURKA has been considered to be a promising target for anti-cancer treatment, clinical trials of AURKA inhibitors such as alisertib (MLN8237) have been conducted at phases I–III. Administration of Alisertib to various tumours has improved time to disease progression, progression-free survival, and the duration of disease stability, which shows modest single-agent anti-tumour activity without leading to significant regression or remission of cancer[66]. Therefore, AURKA inhibitors are beginning to be used in combination therapies[67, 68].

Considering the effect of AURKA inhibitors on mitosis, which induce erroneous chromosome separation, they may induce further chromosomal rearrangements that promote tumour growth, especially in the background where the checkpoint mechanisms are weakened by an *APC* mutation. Thus, we believe that the ability that allows chromosomal reorganization or imbalance of tumour cells is a more important and promising target for cancer therapy. Therefore, we are continuing our efforts to elucidate the detailed molecular mechanism by which *APC* mutations weaken the checkpoint function.

CNAs to restore tumour cell fitness

Although numerical and structural alterations of chromosomes have been believed to promote tumour progression, paradoxically they are also known to decrease cellular fitness and interfere with the proliferation of untransformed cells[4, 5, 69]. It has remained uncertain why cancer cells can have such a heavy mutational burden. Our results demonstrated that *APC* mutations decreased cellular fitness because of adverse effects caused by stabilized β-catenin that blocked AURKA activation. *APC*-mutant cells need to increase AURKA activity to restore fitness rather than to

gain additional growth advantages, which could be a major selection pressure to achieve optimal fitness through the formation of compensatory CNAs.

This kind of view of compensatory mutation has been extensively studied in the field of molecular and microbial evolutions[70, 71, 72]. Here, the deleterious effects of one mutation that causes fitness loss is effectively compensated by its epistatic interaction with a second mutation. Interestingly, in the bacteriophage, the probability of compensatory mutations increase with the severity of the deleterious fitness effect, while compensatory mutations have deleterious effects in a wildtype background[73]. Our observation that chromosome 20 amplification conferred cells a growth advantage only when the APC function was reduced in MCF10A cells demonstrated that cellular fitness was regulated by the balance between the activities of APC and chromosome 20. If a considerable number of chromosome alteration events are driven out of necessity to compensate, this hypothesis may facilitate elucidation of the mechanism of recurrent CNA formation.

Collectively, in this study, we provide an example of compensatory CNAs by identifying a critical relationship between prior mutations (*APC* mutations) and particular CNAs (AURKA-activating CNAs such as human chromosome 20 amplification). This idea can be applied to other cancer types to unravel the precise sequence of events and underlying mechanisms of the formation of cancer type-specific CNAs. Thus, compensatory CNAs that adjust tumour cell fitness represent an important, but previously unappreciated, mechanism that influences the course of cancer genome evolution.

References

1. Beroukhim R, et al. The landscape of somatic copy-number alteration across human cancers. Nature 463, 899-905 (2010).

2. Cancer Genome Atlas N. Comprehensive molecular characterization of human colon and rectal cancer. Nature 487, 330-337 (2012).

3. Myllykangas S, Bohling T, Knuutila S. Specificity, selection and significance of gene amplifications in cancer. Semin Cancer Biol 17, 42-55 (2007).

4. Ben-David U, Amon A. Context is everything: aneuploidy in cancer. Nature reviews Genetics 21, 44-62 (2020).

5. Holland AJ, Cleveland DW. Losing balance: the origin and impact of aneuploidy in cancer. EMBO reports 13, 501-514 (2012).

6. Holland AJ, Cleveland DW. Boveri revisited: chromosomal instability, aneuploidy and tumorigenesis. Nature reviews Molecular cell biology 10, 478-487 (2009).

7. Burrell RA, McGranahan N, Bartek J, Swanton C. The causes and consequences of genetic heterogeneity in cancer evolution. Nature 501, 338-345 (2013).

8. Zhang CZ, et al. Chromothripsis from DNA damage in micronuclei. Nature 522, 179-184 (2015).

9. Leibowitz ML, Zhang CZ, Pellman D. Chromothripsis: A New Mechanism for Rapid Karyotype Evolution. Annual review of genetics 49, 183-211 (2015).

10. Janssen A, van der Burg M, Szuhai K, Kops GJ, Medema RH. Chromosome segregation errors as a cause of DNA damage and structural chromosome aberrations. Science 333, 1895-1898 (2011).

11. Stamos JL, Weis WI. The beta-catenin destruction complex. Cold Spring Harbor perspectives in biology 5, a007898 (2013).

12. Clevers H, Nusse R. Wnt/beta-catenin signaling and disease. Cell 149, 1192-1205 (2012).

13. Ikeda S, Kishida S, Yamamoto H, Murai H, Koyama S, Kikuchi A. Axin, a negative regulator of the Wnt signaling pathway, forms a complex with GSK-3beta and beta-catenin and promotes GSK-3beta-dependent phosphorylation of beta-catenin. The EMBO journal 17, 1371-1384 (1998).

14. Näthke IS, Adams CL, Polakis P, Sellin JH, Nelson WJ. The adenomatous polyposis coli tumor suppressor protein localizes to plasma membrane sites involved in active cell migration. The Journal of cell biology 134, 165-179 (1996).

15. Mimori-Kiyosue Y, Shiina N, Tsukita S. Adenomatous polyposis coli (APC) protein moves along microtubules and concentrates at their growing ends in epithelial cells. The Journal of cell biology 148, 505-518 (2000).

16. Fodde R, et al. Mutations in the APC tumour suppressor gene cause chromosomal instability. Nature cell biology 3, 433-438 (2001).

17. Kaplan KB, Burds AA, Swedlow JR, Bekir SS, Sorger PK, Näthke IS. A role for the Adenomatous Polyposis Coli protein in chromosome segregation. Nature cell biology 3, 429-432 (2001).

18. Draviam VM, Shapiro I, Aldridge B, Sorger PK. Misorientation and reduced stretching of aligned sister kinetochores promote chromosome missegregation in EB1- or APC-depleted cells. The EMBO journal 25, 2814-2827 (2006).

19. Tighe A, Johnson VL, Taylor SS. Truncating APC mutations have dominant effects on proliferation, spindle checkpoint control, survival and chromosome stability. J Cell Sci 117, 6339-6353 (2004).

20. Rusan NM, Peifer M. Original CIN: reviewing roles for APC in chromosome instability. The Journal of cell biology 181, 719-726 (2008).

21. Nishisho I, et al. Mutations of chromosome 5q21 genes in FAP and colorectal cancer patients. Science 253, 665-669 (1991).

22. Kinzler KW, et al. Identification of a gene located at chromosome 5q21 that is mutated in colorectal cancers. Science 251, 1366-1370 (1991).

23. Kinzler KW, Vogelstein B. Lessons from hereditary colorectal cancer. Cell 87, 159-170 (1996).

24. Anderson CB, Neufeld KL, White RL. Subcellular distribution of Wnt pathway proteins in normal and neoplastic colon. Proceedings of the National Academy of Sciences of the United States of America 99, 8683-8688 (2002).

25. Bläker H, Scholten M, Sutter C, Otto HF, Penzel R. Somatic mutations in familial adenomatous polyps. Nuclear translocation of beta-catenin requires more than biallelic APC inactivation. American journal of clinical pathology 120, 418-423 (2003).

26. Amos-Landgraf JM, et al. A target-selected Apc-mutant rat kindred enhances the modeling of familial human colon cancer. Proceedings of the National Academy of Sciences of the United States of America 104, 4036-4041 (2007).

27. Fodde R, Brabletz T. Wnt/beta-catenin signaling in cancer stemness and malignant behavior. Current opinion in cell biology 19, 150-158 (2007).

28. Phelps RA, et al. A two-step model for colon adenoma initiation and progression caused by APC loss. Cell 137, 623-634 (2009).

29. Banks JD, Heald R. Adenomatous polyposis coli associates with the microtubule-destabilizing protein XMCAK. Current biology : CB 14, 2033-2038 (2004).

30. Dikovskaya D, et al. Loss of APC induces polyploidy as a result of a combination of defects in mitosis and apoptosis. Journal of Cell Biology 176, 183-195 (2007).

31. Chen BC, et al. Lattice light-sheet microscopy: imaging molecules to embryos at high spatiotemporal resolution. Science 346, 1257998 (2014).

32. Yamashita N, et al. Three-dimensional tracking of plus-tips by lattice light-sheet microscopy permits the quantification of microtubule growth trajectories within the mitotic apparatus. Journal of biomedical optics 20, 101206 (2015).

33. Mimori-Kiyosue Y, Shiina N, Tsukita S. The dynamic behavior of the APC-binding protein EB1 on the distal ends of microtubules. Current biology : CB 10, 865-868 (2000).

34. Marumoto T, Zhang D, Saya H. Aurora-A - a guardian of poles. Nature Reviews Cancer 5, 42-50 (2005).

35. Lens SMA, Voest EE, Medema RH. Shared and separate functions of polo-like kinases and aurora kinases in cancer. Nature Reviews Cancer 10, 825-841 (2010).

36. Nikonova AS, Astsaturov I, Serebriiskii IG, Dunbrack RL, Jr., Golemis EA. Aurora A kinase (AURKA) in normal and pathological cell division. Cellular and molecular life sciences : CMLS 70, 661-687 (2013).

37. Xia Z, et al. AURKA governs self-renewal capacity in glioma-initiating cells via stabilization/activation of beta-catenin/Wnt signaling. Molecular cancer research : MCR 11, 1101-1111 (2013).

38. Bayliss R, Sardon T, Vernos I, Conti E. Structural basis of Aurora-A activation by TPX2 at the mitotic spindle. Mol Cell 12, 851-862 (2003).

39. Smits R, et al. Apc1638T: a mouse model delineating critical domains of the adenomatous polyposis coli protein involved in tumorigenesis and development. Genes & development 13, 1309-1321 (1999).

40. Fodde R, Smits R. Disease model: familial adenomatous polyposis. Trends in molecular medicine 7, 369-373 (2001).

41. Fearnhead NS, Britton MP, Bodmer WF. The ABC of APC. Human molecular genetics 10, 721-733 (2001).

42. Fumoto K, Kadono M, Izumi N, Kikuchi A. Axin localizes to the centrosome and is involved in microtubule nucleation. EMBO reports 10, 606-613 (2009).

43. Kim SM, et al. Axin localizes to mitotic spindles and centrosomes in mitotic cells. Experimental cell research 315, 943-954 (2009).

44. Ruan K, Ye F, Li CY, Liou YC, Lin SC, Lin SY. PLK1 Interacts and Phosphorylates Axin That Is Essential for Proper Centrosome Formation. PloS one 7, (2012).

45. Kaplan DD, Meigs TE, Kelly P, Casey PJ. Identification of a role for beta-catenin in the establishment of a bipolar mitotic spindle. Journal of Biological Chemistry 279, 10829-10832 (2004).

46. Naso FD, et al. Excess TPX2 Interferes with Microtubule Disassembly and Nuclei Reformation at Mitotic Exit. Cells 9, (2020).

47. Oshima M, Oshima H, Kitagawa K, Kobayashi M, Itakura C, Taketo M. Loss of Apc heterozygosity and abnormal tissue building in nascent intestinal polyps in mice carrying a truncated Apc gene. Proceedings of the National Academy of Sciences of the United States of America 92, 4482-4486 (1995).

48. Hutterer A, Berdnik D, Wirtz-Peitz F, Zigman M, Schleiffer A, Knoblich JA. Mitotic activation of the kinase Aurora-A requires its binding partner Bora. Developmental cell 11, 147-157 (2006).

49. Zhan T, Rindtorff N, Boutros M. Wnt signaling in cancer. Oncogene 36, 1461-1473 (2017).

50. Guinney J, et al. The consensus molecular subtypes of colorectal cancer. Nature medicine 21, 1350-1356 (2015).

51. Naxerova K, et al. Origins of lymphatic and distant metastases in human colorectal cancer. Science 357, 55-60 (2017).

52. Nathanson SD. Insights into the mechanisms of lymph node metastasis. Cancer 98, 413-423 (2003).

53. Takahashi Y, et al. The AURKA/TPX2 axis drives colon tumorigenesis cooperatively with MYC. Annals of oncology : official journal of the European Society for Medical Oncology / ESMO 26, 935-942 (2015).

54. Goos JA, et al. Aurora kinase A (AURKA) expression in colorectal cancer liver metastasis is associated with poor prognosis. British journal of cancer 109, 2445-2452 (2013).

55. Crasta K, et al. DNA breaks and chromosome pulverization from errors in mitosis. Nature 482, 53-58 (2012).

56. Aoki K, et al. Chromosomal instability by beta-catenin/TCF transcription in APC or beta-catenin mutant cells. Oncogene 26, 3511-3520 (2007).

57. Hadjihannas MV, Bruckner M, Jerchow B, Birchmeier W, Dietmaier W, Behrens J. Aberrant Wnt/beta-catenin signaling can induce chromosomal instability in colon cancer. Proceedings of the National Academy of Sciences of the United States of America 103, 10747-10752 (2006).

58. Sasai K, et al. Targeted disruption of Aurora A causes abnormal mitotic spindle assembly, chromosome misalignment and embryonic lethality. Oncogene 27, 4122-4127 (2008).

59. Bienz M, Clevers H. Linking colorectal cancer to Wnt signaling. Cell 103, 311-320 (2000).

60. Clevers H. Wnt/beta-catenin signaling in development and disease. Cell 127, 469-480 (2006).

61. Romagnolo B, et al. Intestinal dysplasia and adenoma in transgenic mice after overexpression of an activated beta-catenin. Cancer research 59, 3875-3879 (1999).

62. Harada N, et al. Intestinal polyposis in mice with a dominant stable mutation of the beta-catenin gene. The EMBO journal 18, 5931-5942 (1999).

63. Janssen KP, et al. APC and oncogenic KRAS are synergistic in enhancing Wnt signaling in intestinal tumor formation and progression. Gastroenterology 131, 1096-1109 (2006).

64. Negrini S, Gorgoulis VG, Halazonetis TD. Genomic instability--an evolving hallmark of cancer. Nature reviews Molecular cell biology 11, 220-228 (2010).

65. Michor F, Iwasa Y, Vogelstein B, Lengauer C, Nowak MA. Can chromosomal instability initiate tumorigenesis? Semin Cancer Biol 15, 43-49 (2005).

66. Tayyar Y, Jubair L, Fallaha S, McMillan NAJ. Critical risk-benefit assessment of the novel anti-cancer aurora a kinase inhibitor alisertib (MLN8237): A comprehensive review of the clinical data. Critical reviews in oncology/hematology 119, 59-65 (2017).

67. Du R, Huang C, Liu K, Li X, Dong Z. Targeting AURKA in Cancer: molecular mechanisms and opportunities for Cancer therapy. Molecular cancer 20, 15 (2021).

68. Goff LW, et al. Phase I study combining the aurora kinase a inhibitor alisertib with mFOLFOX in gastrointestinal cancer. Investigational new drugs 37, 315-322 (2019).

69. Williams BR, et al. Aneuploidy affects proliferation and spontaneous immortalization in mammalian cells. Science 322, 703-709 (2008).

70. Kimura M. The role of compensatory neutral mutations in molecular evolution. J Genet 64, 7-19 (1985).

71. Pal C, Papp B, Lercher MJ. An integrated view of protein evolution. Nature reviews Genetics 7, 337-348 (2006).

72. DePristo MA, Weinreich DM, Hartl DL. Missense meanderings in sequence space: a biophysical view of protein evolution. Nature reviews Genetics 6, 678-687 (2005).

73. Poon A, Chao L. The rate of compensatory mutation in the DNA bacteriophage phiX174. Genetics 170, 989-999 (2005).

74. Mimori-Kiyosue Y, et al. CLASP1 and CLASP2 bind to EB1 and regulate microtubule plus-end dynamics at the cell cortex. The Journal of cell biology 168, 141-153 (2005).

75. Nakamura S, Grigoriev I, Nogi T, Hamaji T, Cassimeris L, Mimori-Kiyosue Y. Dissecting the nanoscale distributions and functions of microtubule-end-binding proteins EB1 and ch-TOG in interphase HeLa cells. PloS one 7, e51442 (2012).

76. Hotta A, et al. Laminin-based cell adhesion anchors microtubule plus ends to the epithelial cell basal cortex through LL5alpha/beta. The Journal of cell biology 189, 901-917 (2010).

77. Shirayoshi Y, Nose A, Iwasaki K, Takeichi M. N-linked oligosaccharides are not involved in the function of a cell-cell binding glycoprotein E-cadherin. Cell Struct Funct 11, 245-252 (1986).

78. Kawasaki Y, et al. Asef, a link between the tumor suppressor APC and G-protein signaling. Science 289, 1194-1197 (2000).

79. Takahashi N, Ishihara S, Takada S, Tsukita S, Nagafuchi A. Posttranscriptional regulation of alpha-catenin expression is required for Wnt signaling in L cells. Biochem Bioph Res Co 277, 691-698 (2000).

80. Yamamoto H, et al. Axil, a member of the Axin family, interacts with both glycogen synthase kinase 3 beta and beta-catenin and inhibits axis formation of Xenopus embryos. Mol Cell Biol 18, 2867-2875 (1998).

81. Pronobis MI, Deuitch N, Posham V, Mimori-Kiyosue Y, Peifer M. Reconstituting regulation of the canonical Wnt pathway by engineering a minimal beta-catenin destruction machine. Molecular biology of the cell 28, 41-53 (2017).

82. Widlund PO, et al. XMAP215 polymerase activity is built by combining multiple tubulin-binding TOG domains and a basic lattice-binding region. Proceedings of the National Academy of Sciences of the United States of America 108, 2741-2746 (2011).

83. Oshima H, Oshima M, Kobayashi M, Tsutsumi M, Taketo MM. Morphological and molecular processes of polyp formation in Apc(Delta 716) knockout mice. Cancer research 57, 1644-1649 (1997).

84. Yokoyama A, et al. The C-terminal domain of the adenomatous polyposis coli (Apc) protein is involved in thyroid morphogenesis and function. Medical molecular morphology 44, 207-212 (2011).

85. Sells TB, et al. MLN8054 and Alisertib (MLN8237): Discovery of Selective Oral Aurora A Inhibitors. ACS medicinal chemistry letters 6, 630-634 (2015).

86. Bigagli E, et al. DNA copy number alterations, gene expression changes and disease-free survival in patients with colorectal cancer: a 10 year follow-up. Cell Oncol (Dordr) 39, 545-558 (2016).

87. Uchi R, et al. Integrated Multiregional Analysis Proposing a New Model of Colorectal Cancer Evolution. PLoS genetics 12, e1005778 (2016).

88. Shiraishi Y, et al. An empirical Bayesian framework for somatic mutation detection from cancer genome sequencing data. Nucleic acids research 41, e89 (2013).

89. Van Loo P, et al. Allele-specific copy number analysis of tumors. Proceedings of the National Academy of Sciences of the United States of America 107, 16910-16915 (2010).

90. Debnath J, Muthuswamy SK, Brugge JS. Morphogenesis and oncogenesis of MCF-10A mammary epithelial acini grown in three-dimensional basement membrane cultures. Methods 30, 256-268 (2003).

91. Soule HD, et al. Isolation and characterization of a spontaneously immortalized human breast epithelial cell line, MCF-10. Cancer research 50, 6075-6086 (1990).

92. Cowell JK, LaDuca J, Rossi MR, Burkhardt T, Nowak NJ, Matsui S. Molecular characterization of the t(3;9) associated with immortalization in the MCF10A cell line. Cancer genetics and cytogenetics 163, 23-29 (2005).

93. Jonsson G, et al. High-resolution genomic profiles of breast cancer cell lines assessed by tiling BAC array comparative genomic hybridization. Genes, chromosomes & cancer 46, 543-558 (2007).

94. Zientek-Targosz H, et al. Transformation of MCF-10A cells by random mutagenesis with frameshift mutagen ICR191: a model for identifying candidate breast-tumor suppressors. Molecular cancer 7, 51 (2008).

95. Marella NV, Malyavantham KS, Wang J, Matsui S, Liang P, Berezney R. Cytogenetic and cDNA microarray expression analysis of MCF10 human breast cancer progression cell lines. Cancer research 69, 5946-5953 (2009).

Figure 1 Kawasaki et al.

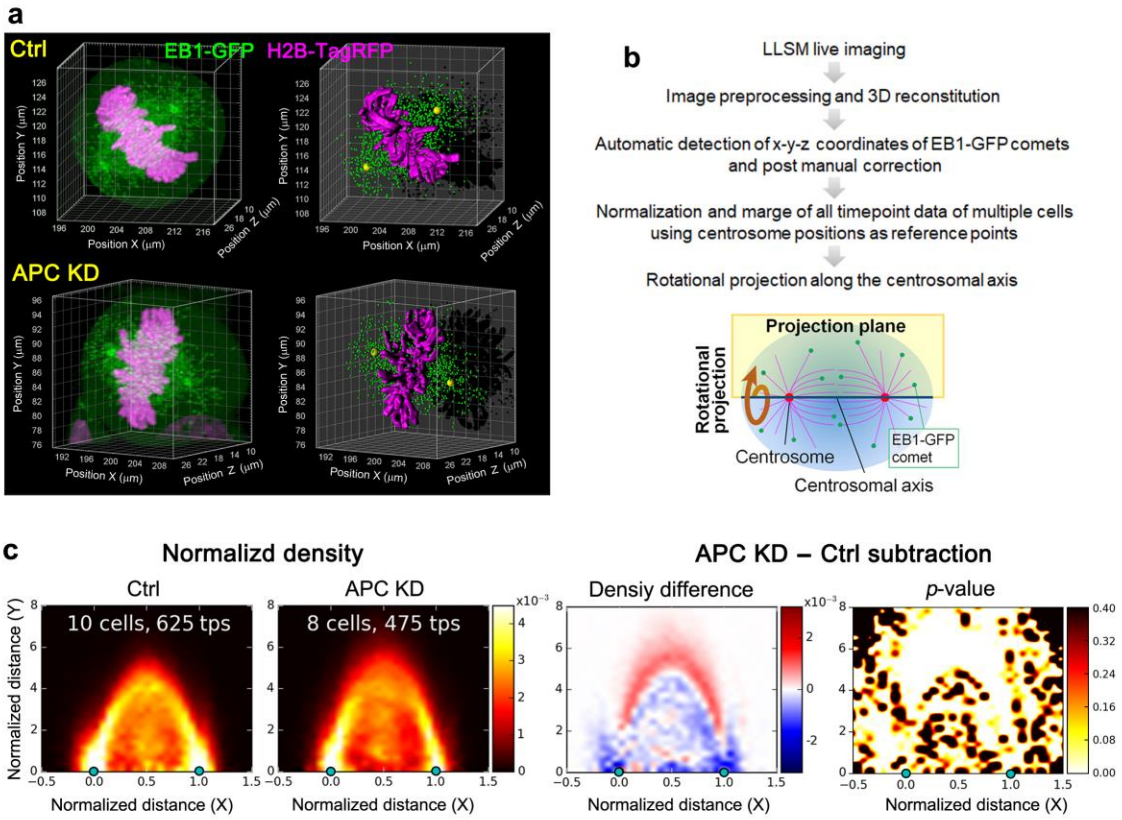

Fig. 1 | Identification of the site affected by APC depletion and regulation of AURKA by APC. (**a**) Three-dimensional representation of control (Ctrl) and APC-depleted (APC KD) mitotic HeLa cells that expressed EB1-GFP and H2B-TagRFP as visualized by lattice light sheet microscopy. Original images (left) and examples of automated detection of EB1-GFP positions and chromosome surfaces (right) are shown. See also Movies 1–3. (**b**) Procedure for quantitative analysis of the timelapse 3D data. The rotational projection method is shown diagrammatically at the bottom. (**c**) Rotationally projected density map of control and APC-depleted cells (left). The centrosome positions are indicated by green dots at positions 0.0 and 1.0 on the x-axis. The number of cells and time points (tps) in timelapse videos are indicated in the panel. A density difference map (middle) and p-value map (right) are shown.

Figure 2 Kawasaki et al.

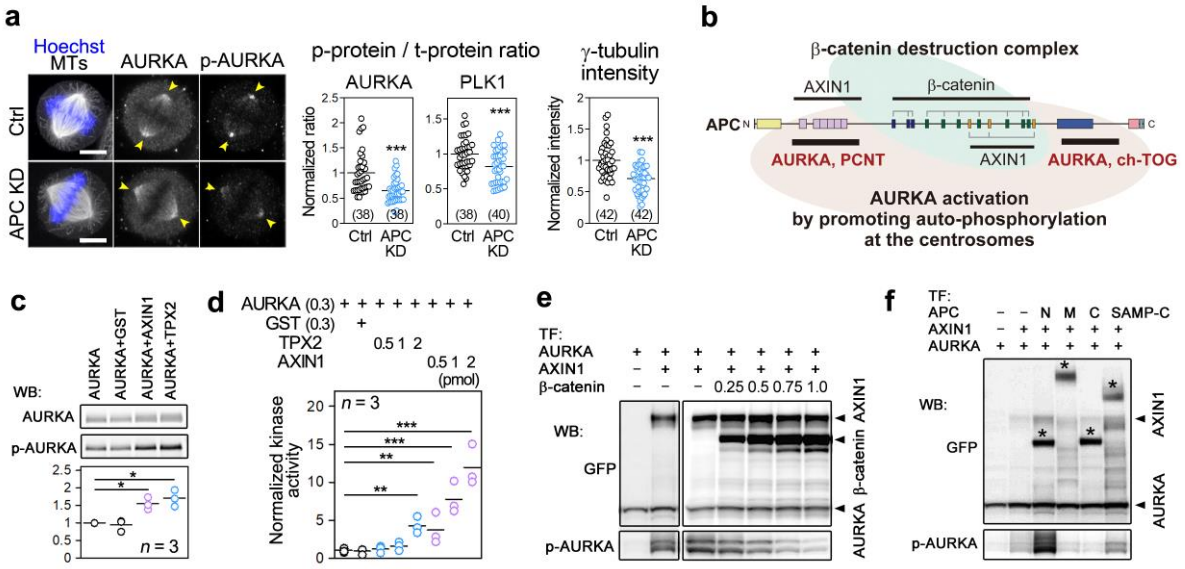

Fig. 2 | Regulation of AURKA by APC, AXIN1, and β-catenin. (**a**) Immunostaining of AURKA, p-T288 AURKA (left), and microtubules (MTs) with Hoechst 33342 to stain DNA (left). See also Extended Data Table 1. Ratios of fluorescence intensities (phosphorylated vs. total protein) of AURKA (T288) and PLK1 (T210), and fluorescence intensities of γ-tubulin at centrosomes are shown (right). Scale bars: 5 μm. (**b**) Binding sites for centrosomal proteins and components of the β-catenin destruction complex. (**c**) *In vitro* AURKA autophosphorylation at T288 detected by western blotting. (**d**) *In vitro* kinase assay of AURKA autophosphorylation. (**e, f**) HEK293T cells were transfected with GFP-fused AURKA, AXIN1, β-catenin, and APC fragments (see Extended Data Figure 3a) as indicated and then subjected to western blotting using the indicated antibodies. APC bands are marked with asterisks. Note that the phosphorylated AURKA band always appeared as multiple bands and AXIN1 levels were increased when coexpressed with binding APC fragments. For uncropped versions of blots, see Extended Data Table 2. **P < 0.01; ***P < 0.001, Student's t-test (a), Tukey–Kramer method (c, d)

Figure 3 Kawasaki et al.

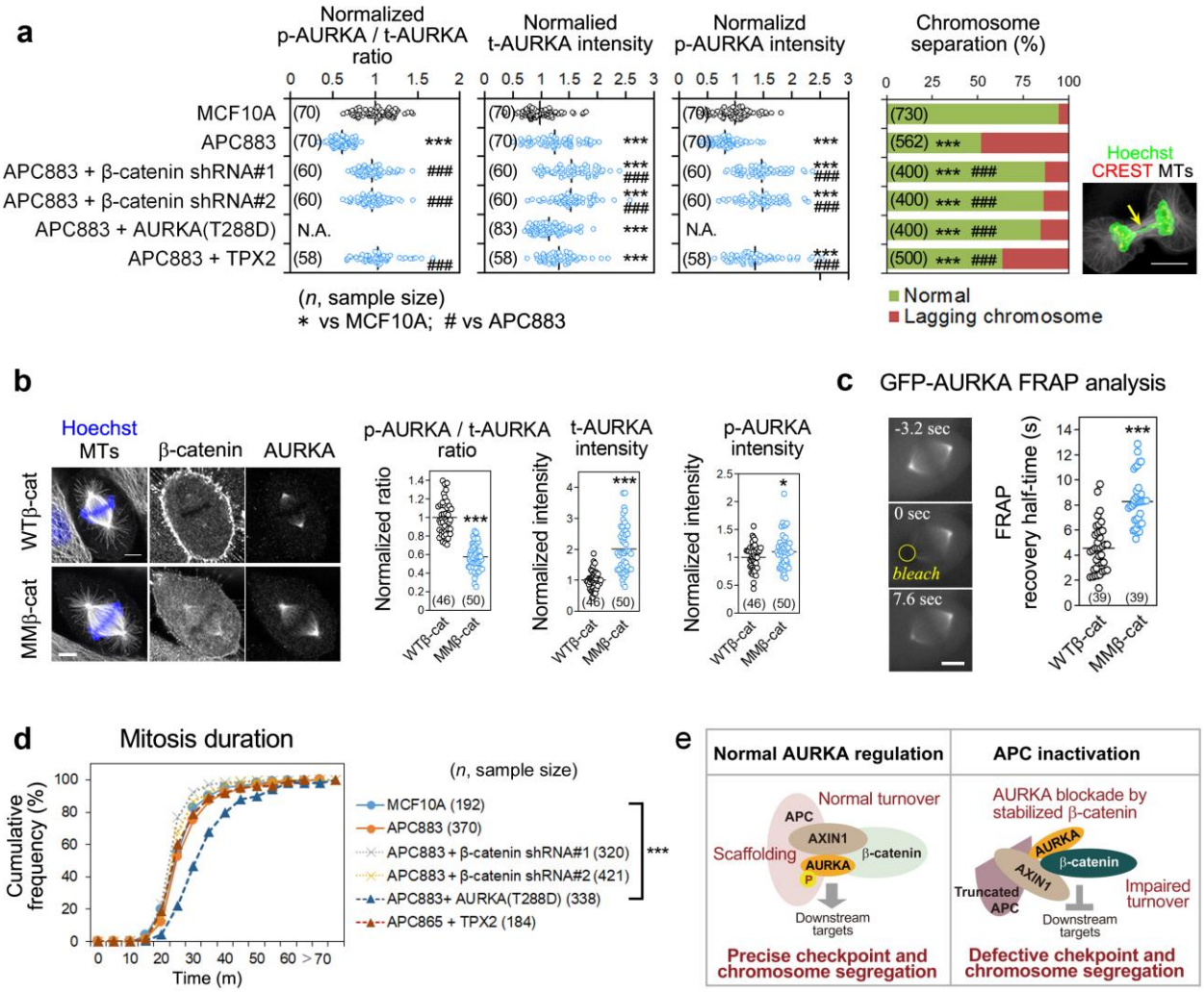

Fig. 3 | Stabilized β-catenin blocks AURKA activation and the checkpoint function. (**a**) AURKA status at centrosomes obtained from immunofluorescence images. See also Extended Data Table 1. Total AURKA protein levels (t-AURKA), autophosphorylated AURKA levels (p-AURKA), the auto-phosphorylation ratio (p-AURKA/t-AURKA ratio), and mitotic error rate in parental MCF10A cells that expressed full-length APC, APC883 cells, and cell lines derived from APC883 cells are shown as indicated. Mitotic errors were monitored by generation of lagging chromosomes (lower right). (**b**) Representative images of immunostained MCF10A cells

that expressed myc-WTβ-catenin or myc-MMβ-catenin (left) and signal intensity analysis of AURKA (right). (**c**) FRAP analysis of GFP-AURKA in cells that expressed WT β-catenin or MMβ-catenin. Representative images (left) and average FRAP recovery half-time (right) are shown. See also Extended Data Table 1. (**d**) Duration of mitosis in each cell line shown as a cumulative histogram. See also Movies 4–6 and Extended Data Table 1. (**e**) Schematic diagram of AURKA regulation by the APC/AXIN1/β-catenin complex. Scale bars: 5 μm. For (a), ***$P < 0.001$ vs. MCF10A, $^{###}P < 0.001$ vs. APC883, Student's t-test. ***$P < 0.001$, Student's t-test (b, c), Tukey–Kramer method (a, d).

Figure 4 Kawasaki et al.

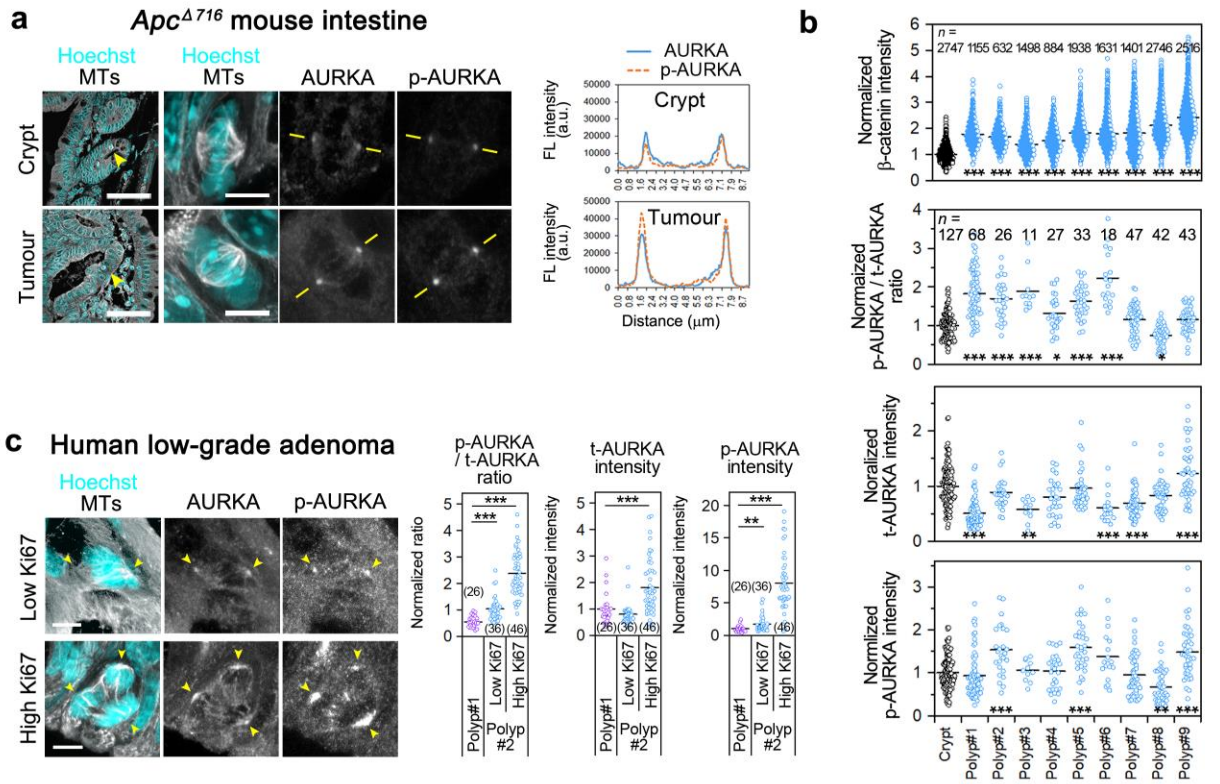

Fig. 4 | AURKA activation in mouse/human tumours. (**a**) Representative images of mitotic cells in *Apc*$^{\Delta 716}$ mouse intestines stained for AURKA, p-T288 AURKA (left), microtubules (MTs), and DNA with Hoechst 33342 (left), and line profiles of fluorescence intensities along the centrosomal axis (right). (**b**) Quantitative analysis of immunofluorescence signals of AURKA in crypts and tumour tissues of nine polyps. See also Extended Data Fig. 6. (**c**) Representative images of mitotic cells in human polyp #2 (left). See also Extended Data Fig. 7 and Extended Data Table 1. Quantitative analysis of immunofluorescence signals of AURKA in polyp #1 without an APC mutation and two regions in polyp #2. Scale bars: 50 μm (a, left), 5 μm (a, middle; c). *P < 0.05; **P < 0.01; ***P < 0.001; Tukey–Kramer test (b, c).

Figure 5 Kawasaki et al.

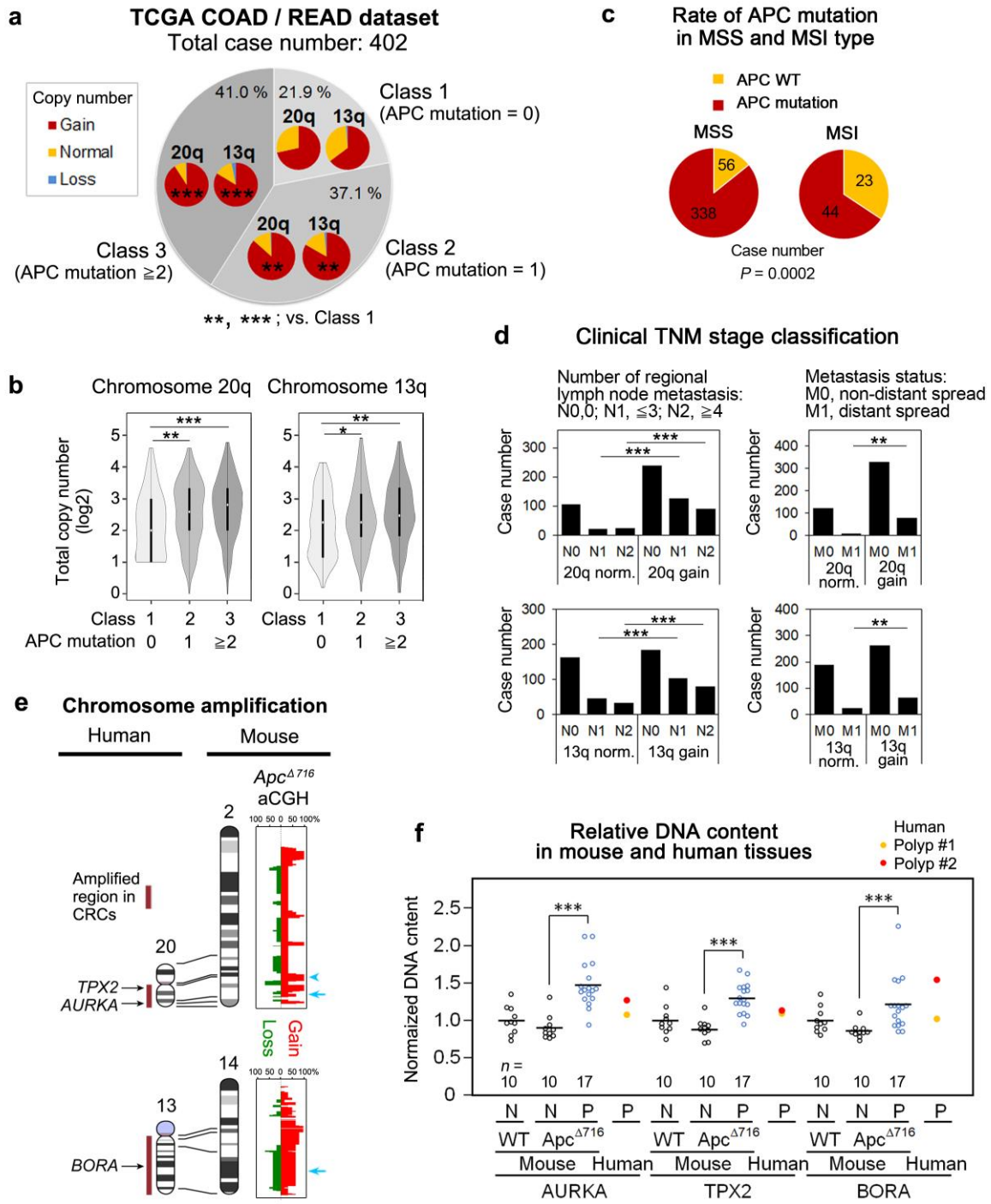

Fig. 5 | Recurrent CNAs in *APC*-mutant human CRCs and mouse tumours. (**a–d**) Reanalysis of The Cancer Genome Atlas (TCGA)-CRC [colon adenocarcinoma (COAD) + rectum

adenocarcinoma (READ)] dataset. Correlation between the *APC* mutation number and copy number alteration of chromosomes 20q and 13q in human CRCs (a). Distribution of total copy numbers of chromosomes 20q and 13q in the three classes as shown by a violin plot (b). Rate of *APC* mutations in microsatellite-stable (MSS) and microsatellite-unstable (MSI) subgroups (c). Clinical tumour-node-metastasis (TNM) stage classification of patients with or without 20q or 13q amplification (d). (**e**) Synteny alignment of human chromosomes 20 and 13 and mouse chromosomes 2 and 14, and aCGH analysis of $Apc^{\Delta 716}$ mouse polyps shown as frequency plots. Red and green indicate regions of gain and loss, respectively. Positions of mouse *Tpx2* (arrowhead, top), *Aurka* (arrow, top), *Bora* (arrow, bottom) are shown. See also Extended Data Fig. 8. (**f**) Relative DNA content of *AURKA*, *TPX2*, and *BORA* genes in normal crypt tissues (N) of WT (N) and $Apc^{\Delta 716}$ mice and polyps (P) of $Apc^{\Delta 716}$ mice and humans (polyp #1 and #2). Seventeen polyps from four $Apc^{\Delta 716}$ mice were analysed. See also Extended Data Fig. 7. *P < 0.05; **P < 0.01; ***P < 0.001; Fisher's exact test (a, c, d); Kruskal–Wallis rank-sum test (b); Student's t-test (f).

Figure 6 Kawasaki et al.

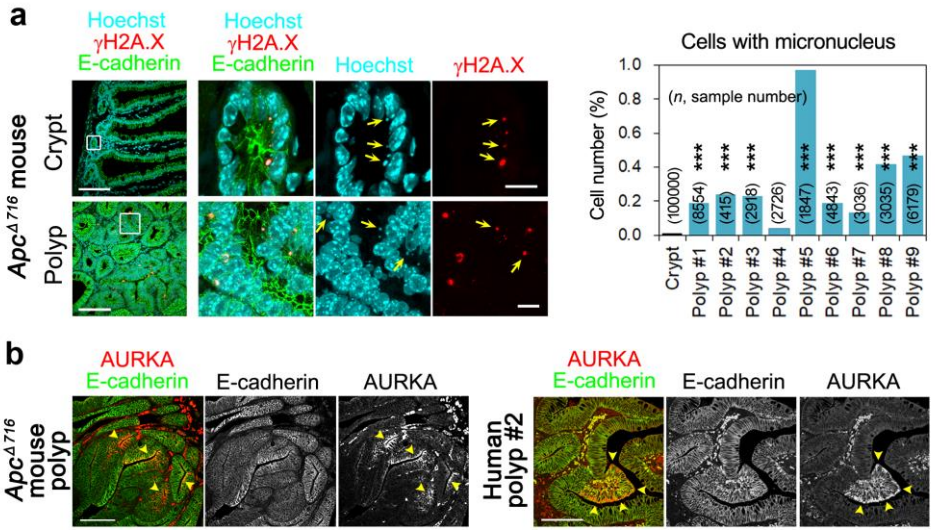

Fig. 6 | DNA damage and local increases of AURKA levels in intestinal tumours. (**a**) Representative images of micronuclei positive for γH2A.X in a crypt and tumour from an *Apc*$^{\Delta 716}$ mouse (arrows at the left). Percentages of cells with γH2A.X-positive micronuclei in crypts and tumour tissues in each polyp (right). (**b**) Examples of patchy regions with intense AURKA staining in an *Apc*$^{\Delta 716}$ mouse polyp (left) and human polyp #2 (right). Scale bars: 100 μm (a, left; b) and 10 μm (c, right). ***P < 0.001; Fisher's exact test.

Figure 7 Kawasaki et al.

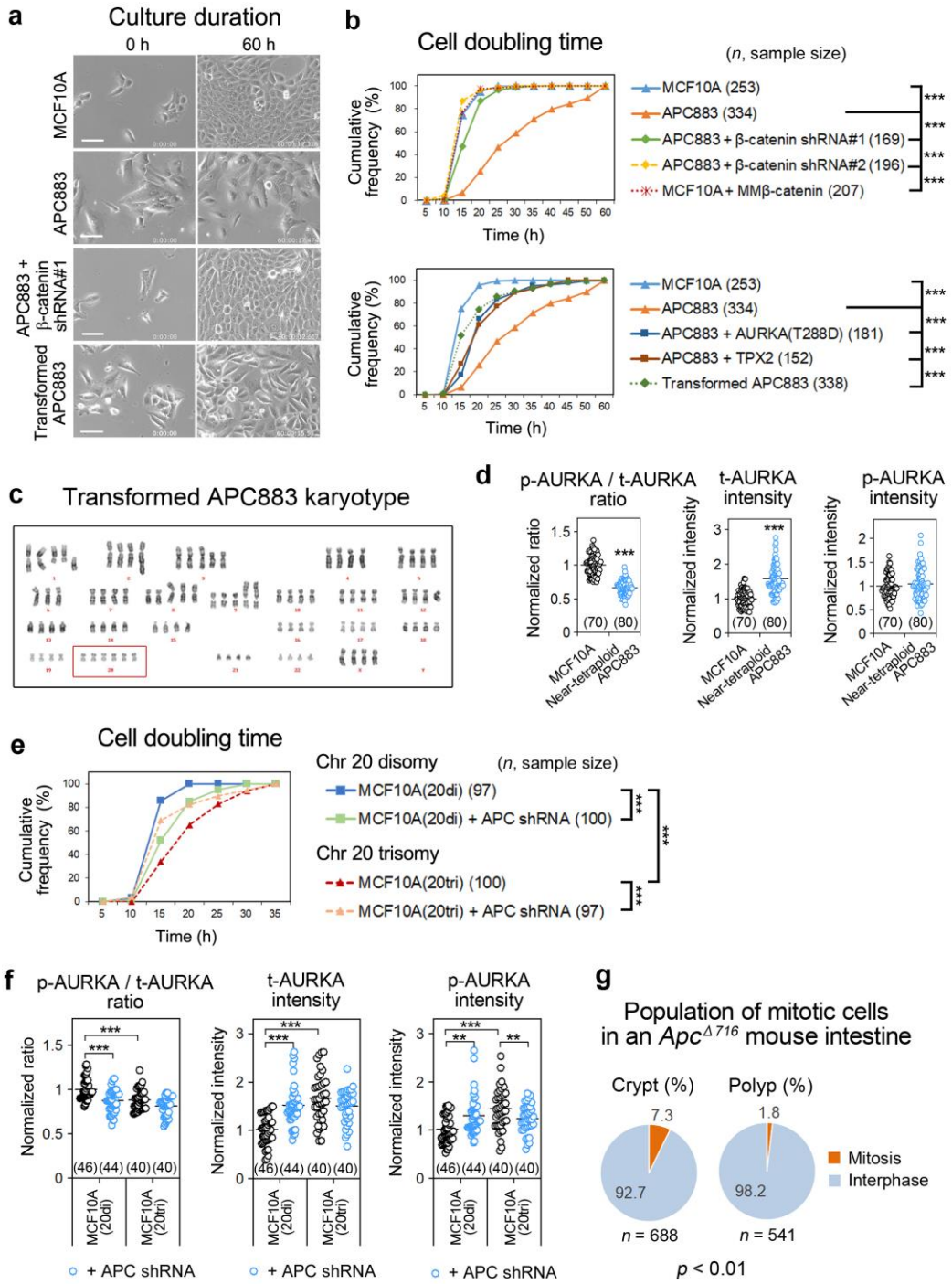

Fig. 7 | Requirement of AURKA activity for proliferation of *APC*-mutant cells. (**a**) Selected images from phase contrast timelapse videos of the indicated cell lines. The first frames (0 h) and

frames at 60 hours later (60 h) are shown. See also Movies 4–6 and Extended Data Table 1. (**b**) Duration of the doubling time of each cell line as shown in a cumulative histogram. (**c**) Representative images of the karyotype of a spontaneously appeared transformed APC883 cells that contained a near tetraploid karyotype with six copies of chromosome 20 (red box). See also Extended Data Fig. 5. (**d**) AURKA signal levels at the centrosome in parental MCF10A cells and transformed APC883 cells. See also Extended Data Table 1. (**e, f**) Duration of the doubling time as shown in a cumulative histogram (e), and AURKA signal levels at the centrosome (f) in each cell line carrying different number of chromosome 20. See also Movie 7 and Extended Data Table 1. (**g**) Population of mitotic cells in *Apc*$^{\Delta 716}$ mouse intestines used to estimate the cell cycle rate. See also Extended Data Table 1. Scale bars: 20 μm. ***P < 0.001 vs. APC883, the Tukey–Kramer method (b, e, f); ***P < 0.001, Student's t-test (d,); ***P < 0.001, the chi-squared test (g).

Figure 8 Kawasaki et al.

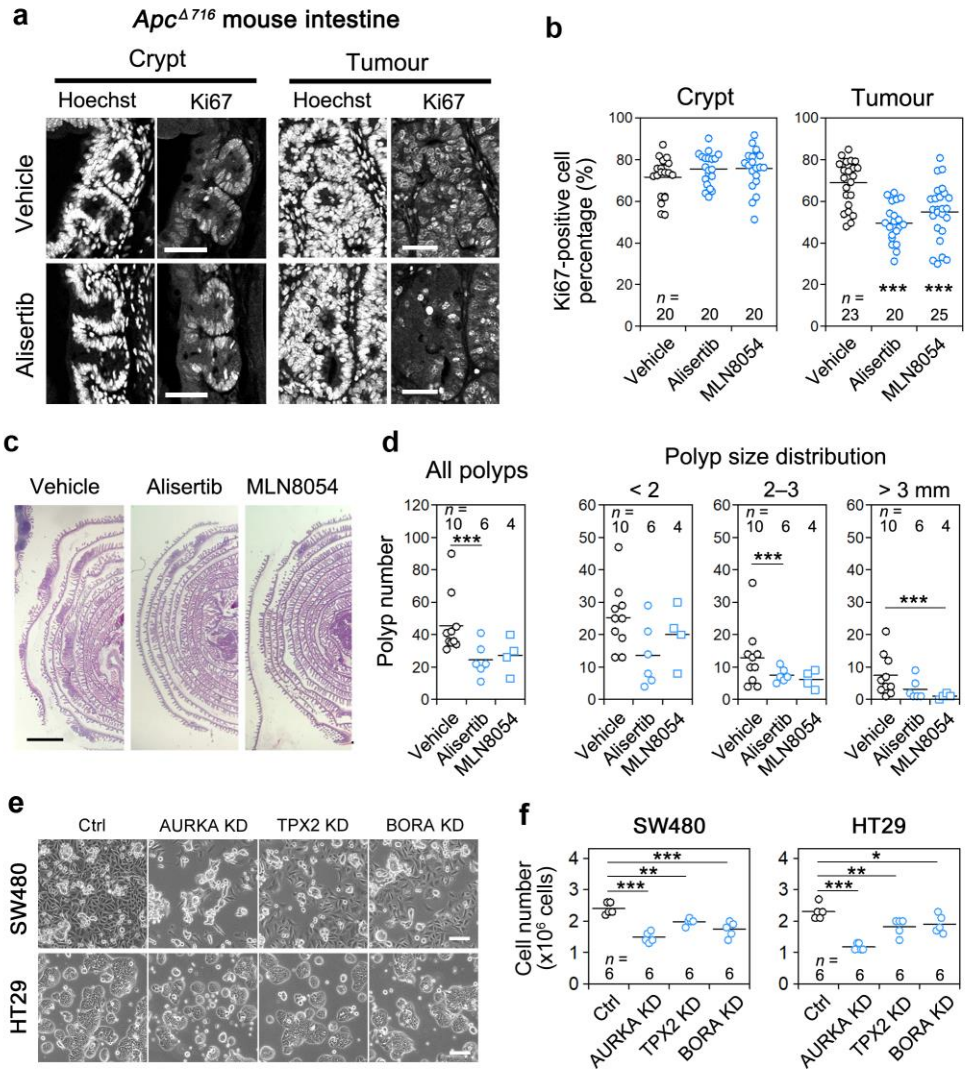

Fig. 8 | Requirement of AURKA activity for tumour cell growth. (**a, b**) Effect of AURKA inhibitors on proliferative activity of mouse intestinal tissues. *Apc*$^{\Delta 716}$ mice were treated with the vehicle or AURKA inhibitors (20 mg/kg alisertib or 30 mg/kg MLN8054) for 14 consecutive days. Representative images of Ki67-labelled tissue sections from *Apc*$^{\Delta 716}$ mice treated with the vehicle or alisertib (a). See also Extended Data Table 1. Analysis of the Ki67-positive cell population (b). (**c, d**) Effect of AURKA inhibitors on polyp development in *Apc*$^{\Delta 716}$ mice which were treated with the vehicle or AURKA inhibitors for 28 consecutive days. Examples of HE-

stained sections of intestines from vehicle- or AURKA inhibitor-treated *Apc*$^{\Delta 716}$ mice (c). Analysis of the polyp number and size distribution in the intestines of vehicle- or AURKA inhibitor-treated *Apc*$^{\Delta 716}$ mice (d). (**e, f**) Effect of depletion of AURKA, TPX2, or BORA on growth of CRC cells. Representative images of the cell culture (e). Analysis of the number of cells (f). Scale bars: 50 μm (a); 2 mm (c); 10 μm (c). ***$P < 0.001$ vs. APC883, the Tukey–Kramer method (b, d, f).

Figure 9 Kawasaki et al.

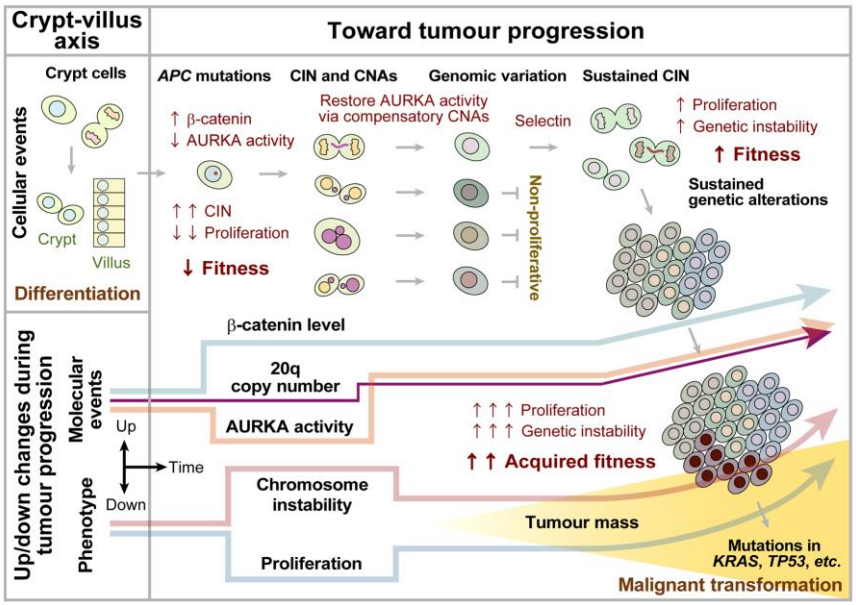

Fig. 9 | Model of the steps for malignant transformation during early tumourigenesis. The normal crypt–villus axis and tumour progression pathway are divided and cell phenotypes are illustrated at the top. The time course of changes in molecular activities and cell/tumour phenotypes is shown at the bottom as diagrammatic line plots. Upon APC inactivation, the CIN that results from AURKA dysregulation generates cells with various chromosomal aberrations and confers a fitness penalty[4]. Some cells restore fitness via AURKA-activating CNAs, which may contribute to the formation of *APC*-mutant cancer-specific CNAs.

Methods

Cell culture and treatment

All cell lines tested negative for mycoplasma contamination. Parental HeLa cell line was authenticated by Bio-Synthesis Inc (Cell Culture STR Profiling and Comparison Analysis (Cat. No.:CL1003). Other cell lines used were obtained from reliable distributors. HeLa cells and HeLa cells expressing EB1-GFP and H2B-TagRFP (clone A1) were maintained as previously described[74, 75]. A parental MCF10A cell line and an MCF10A cell line with the *APC* gene knocked out (MCF10A cells $APC^{-/-}$) were obtained from Sigma-Aldrich-Aldrich (CLLS1069, St. Louis, MO, USA), and cultured in as described previously[76]. The $APC^{-/-}$ cells, which were generated by zinc finger nuclease (ZFN) technology, are homozygous for a 17 bp deletion (GCAGCCCAGATTGCCAA) in the endogenous *APC* gene at 2650-2666 bp of transcript variant 3 (NM_000038). This mutation results in a truncated 883-amino acid APC protein followed by an unrelated 21 amino acid sequence at its C-terminus (SHGRSVSHSYLSGRQKFWVYH). In this paper we refer to this cell line as APC883. The HEK293-based Lenti-X 293T (HEK293T) cell line was obtained from Takara Bio (Shiga, Japan) and was cultured in DMEM (10566024, Thermo Fisher Scientific/Gibco, Waltham, MA, USA) supplemented with 10% FCS at 37°C in a 5% CO_2 atmosphere. Colorectal cancer cell lines SW480 (CCL-228) and HT-29 (HTB-38) were obtained from ATCC (Manassas, VA, USA) and cultured in Leibovitz's L-15 Medium (11415064, Thermo Fisher Scientific/Gibco) supplemented with 10% FCS at 37°C without CO_2, and McCoy's 5a Medium (16600082, Thermo Fisher Scientific/Gibco) supplemented with 10% FCS at 37°C in a 5% CO_2 atmosphere, respectively. Mouse embryonic fibroblasts (MEFs) of wild-type C57BL/6 mice and homozygous Apc^{1638T}

mice were isolated from embryonic day (E) 13.5 embryos, and were cultured in DMEM supplemented with 10% FCS in a 5% CO_2 atmosphere. The number of cells was counted using an automated cell counter (Countess; Invitrogen, Carlsbad, CA, USA).

Lattice light sheet microscopy and data analysis

Three-dimensional live imaging by lattice light sheet microscopy and quantitative data analysis were performed as described previously[31, 32]. Briefly, timelapse images of HeLa cells that stably expressed EB1-GFP and H2B-TagRFP (clone A1)[75] were collected at 0.755-s intervals for EB1-GFP only single channel imaging, 1.550-s intervals for EB1-GFP and H2B-TagRFP dual channel imaging in fast scanning mode (3D voxel pitch: 0.100 × 0.100 × 0.217 μm), or 10.000-s intervals for EB1-GFP and H2B-TagRFP dual channel imaging in high resolution mode (3D voxel pitch: 0.100 × 0.100 × 0.195 μm). The former data were used for quantitative analyses and the latter data were used to visualize mitosis progression. The data were displayed in 3D and processed using Imaris software (Bitplane, Zurich, Switzerland). Supplementary video editing of projected images exported from Imaris and image processing were performed using ImageJ software, QuickTime software (Apple. Cupertino, CA, USA), and Adobe Photoshop software (Adobe, San Jose, CA, USA).

To interpret multidimensional data, images were processed for visualization and mathematical computation. The XYZ coordinate positions of EB1-GFP comets were determined automatically. The results are presented as spots or density, or analysed mathematically using a program developed with MATLAB (MathWorks, Natick, MA, USA) as described previously[32] and Python using libraries NumPy, Math, and Matplotlib. An EB1-GFP comet density map (Fig. 1b) was created from the 2D rotational projected comet numbers and the volume associated with the 2D grid. To create a 2D rotational projection of all comets, the coordinates of comets and

centrosomes were first transformed so that the spindle axis (vector that connected the two centrosomes) aligned with the x-axis of the Cartesian coordinate. Then, all comet points were rotated around the x-axis and projected onto an arbitrary 2D plane with its normal vector orthogonal to the spindle axis. The result was a half spindle that consisted of comets and centrosomes in 2D coordinates. Before assembling comet points from all cells, the x-coordinates of 2D comets were rescaled so that the inter-centrosomal distance was one. Then, a regular 2D grid that covered all comet spots was created and the number of comets in each grid element was counted. Average comet density of each element was calculated by normalizing the number of comets with i) the timelapse duration and ii) calculation of the 3D volume that corresponded to each grid element. The latter is a function of distance from the spindle axis and is expressed as $v=\pi h^2 w(2n-1)$ where $n=1,2,3,...,Ny$ with Ny that represents the total number of grid elements perpendicular to the spindle axis. w and h are the width and height of the elements, respectively. For cell type comparison, comet density was normalized so that the summed density of all elements was one. Normalized density was then rescaled by the global maximum to produce a value between zero and one. Rescaled normalized comet density of each element and interpolated density values of in-between grid elements were coded by colour and plotted. Because the centrosomes had much higher densities relative to other regions, we imposed an upper cutoff colour value to better illustrate the density variation of non-centrosomal regions. The density difference graph was constructed by the difference between the normalized density of each grid element of APC KD and control cells. A significance test of the density difference was performed by the two-sided t-test to obtain the *p*-value. The inputs for the test were the mean and variance value for each grid of the density map. The output is the *p*-value for each grid. The code was deposited in Github

(https://github.com/wxchew/cometdensity/blob/master/2DProjectedCometDensity.ipynb).

Antibodies and immunolabeling

No untested antibody was used. Rat anti-E-cadherin mAb (ECCD-2[77]) was a kind gift from Dr. M. Takeichi (RIKEN CDB). The following commercial primary antibodies were used: mouse anti-APC (Ab-1) mAb for western blotting, clone FE9 (OP44; Lot# D00138185; EMD Millipore/Calbiochem, Billerica, MA, USA); mouse anti-Aurora A mAb, clone 35C1 (ab13824; Lot# GR121501-2; Abcam, Cambridge, UK); rabbit anti-Aurora A (phospho T288) polyclonal antibody (pAb), (ab195748, Lot# GR212301-1; Abcam); rabbit phospho-Aurora A (Thr288)/Aurora B (Thr232)/Aurora C (Thr198) (D13A11) mAb (#2914; Lot# 3; CST, Danvers, MA, USA); mouse anri-PLK1 mAb, clone 36-298 (ab17057; Lot# GR136555-1; Abcam); rabbit anti-PLK1 (phospho T210) mAb, clone EPNCIR167 (ab155095; Lot# YJ092901CS; Abcam); rabbit anti-AXIN1 mAb, clone C76H11 (#2087; Lot# 4; CST); purified human anti-Centromere Protein IgG (CREST) (15-235; Lot# 441.13BK.20; Antibodies Incorporated, Davis, CA, USA); rabbit anti-β-catenin pAb (C2206; Lot# 059K4754; Sigma-Aldrich); mouse anti-β-catenin mAb, clone 14 (610154; Lot# 5113978; BD Transduction Lab.); rabbit anti-Ki67 pAb (ab15580; Lot# GR264768-1; abcam); rabbit anti-TPX2 pAb (HPA005487; Lot# A104169; Sigma); mouse anti-TPX2 mAb, clone 18D5-1 (ab32795; Lot# GR245658-1; abcam); mouse anti-α-tubulin, clone DM1A (T9026; Lot# 078K4763; Sigma-Aldrich); rat anti-tubulin mAb, clone YL1/2 (ab6160; Lot# GR57687-1; Abcam); rabbit anti-γ-tubulin pAb (ab11320; Lot# 628882; Abcam); mouse anti-γ-tubulin mAb, clone GTU-88 (T6557; Lot# 079K4861; Sigma-Aldrich); mouse anti-GAPDH antibody-loading control (HRP), clone mAbcam 9484 (ab9482; Lot# GR149747-1; Abcam); rabbit anti-GFP, HRP-conjugated (598-7; Lot# 002; MBL, Aichi, Japan); mouse anti-GST, clone B-14 (sc-138; Lot# K1808; Santa Cruz Biotechnology); mouse anti-penta-His

antibody (34660; Lot# 136244018; Qiagen); mouse anti-Myc tag mAb, clone 4A6 (05-724; Lot# DAM1724025; Millipore); mouse anti-Myc tag mAb, clone 4A6, peroxidase-conjugated (16-213; Lot# DAM1646292; Millipore); Hoechst 33342 solution (346-07951; Lot# FN027; Dojin, Japan) was used as a nuclear marker. Immunofluorescent staining of fixed cultured cells and western blotting were performed as described previously[74, 75, 76]. Intestinal tissues from 16-weeks old *Apc*$^{\Delta 716}$ mice and human adenomas were fixed in formalin and processed for paraffin-embedding and sectioning as described previously[47]. Antigen retrieval for β-catenin (610154, BD), E-cadherin (ECCD-2), AURKA, phosphor-AURKA(T288) , TPX2, Ki67 and anti-α-tubulin (YL1/2) immunostaining was performed by boiling sections for 30 min in Tris-EDTA pH 9.0.

cDNAs, plasmids and RNA interference

The APC cDNA used was described previously[78]. Wild-type mouse β-catenin and dominant-stable β-catenin (MMβ-catenin), in which the NH_2-terminal four Ser/Thr residues recognized by GSK-3β were substituted for Ala[79] were gifts from Dr. A. Nagafuchi (Nara Medical University). A human AXIN1 cDNA was PCR cloned from MCF10A cells. cDNAs for rat AXIN1 were described previously[13, 80]. The following plasmids were obtained: pWZL Neo Myr Flag AURKA (addgene plasmid # 20427), a gift from William Hahn & Jean Zhao; mEmerald-TPX2-N-10 (addgene plasmid #54285) and mEmerald-Beta-Catenin-20 (mouse) (addgene plasmid #54017), gifts from Michael Davidson. AURKA(T288D) mutation was introduced by PCR engineering. EGFP-fused APC, β-catenin, AXIN1 and AURKA were expressed by inserting these cDNAs into pEGFP-C (Takara/Clontech). Transient transfection of cells with plasmids was performed using Effectene transfection reagent (Qiagen, Germany).

Lentiviral vectors expressing genes of interest under EF1α promoters (pLVSIN-EF1a-IRES-pur, pLVSIN-EF1a-IRES-bsr) were described previously[75]. Myc-tagged AURKA, AURKA(T288D), TPX2, WTβ-catenin and MMβ-catenin were generated by PCR engineering and inserted into pLVSIN-EF1a-IRES series vectors. Lentiviral vectors expressing shRNAs against human *APC* under U6 promoters (pLVSIN-U6-pur, bsr) were described previously[81]. The target sequences of shRNAs for human *AURKA*-related genes were as follows: *AURKA*, CAGGACCTGTTAAGGCTACAG; *TPX2*, CGGTAGTGATAAAAGCTCA and *BORA*, GGTTGATCCTATAGAGATA. The following lentiviral plasmids were obtained: pLKO.1 puro shRNA beta-catenin (addgene plasmid #18803, referred to in this study as β-catenin shRNA#1), a gift from Bob Weinberg; pLKO.1.sh.beta-catenin.2279 (addgene plasmid #19762, referred to in this study as β-catenin shRNA#2), a gift from William Hahn.

Lentiviral gene transfer

Lentiviruses carrying genes of interest were generated in HEK293T(Lenti-X) cells (Takara) using Lentiviral High Titer Packaging Mix (Takara) as described previously[75]. Cells were infected for 24 h with virus in the presence of 10 mg/ml polybrene (Santa Cruz Biotechnology), washed, and allowed to recover for 48 h before selection with appropriate antibiotics. For selection of gene-transduced cells, Puromycin (InvivoGen, San Diego, CA, USA) and Blasticidin S (InvivoGen) were used for selection of the *bsr* resistance gene. HeLa and CRC cells infected with APC shRNA/pLVSIN-U6-pur were maintained in 10-20 μg/ml puromycin. MCF10A cells transfected with cDNA and shRNA were maintained in media containing appropriate concentrations of selection drugs: APC883 + AURKA(T288D), 0.05 μg/ml Blasticidin S; APC883 + β-catenin shRNA#1, 10 μg/ml puromycin; APC883 + β-catenin shRNA#2, 1 μg/ml puromycin; APC883 + TPX2, 0.01 μg/ml puromycin; MCF10A(20di) and MCF10A(20tri) +

APC shRNA, 10 μg/ml puromycin. To screen for genes that are able to stimulate proliferation of APC883 cells as a results of rescue of mitotic defects and delayed doubling time, APC883 cells were screened following transfection by continuous culture for more than a month without drug selection, allowing their unconstrained proliferation. For prolonged culture, the rescued cells were maintained in media containing appropriate selection drugs as described above.

Proteins

For bacterial expression, DNA fragments encoding APC proteins were inserted into pGEX-5X-1 (GE Healthcare Life Sciences, Pittsburgh, PA, USA). For *in vitro* transcription and translation reaction, AURKA cDNA was inserted into pcDNA3.1 (Invitrogen) and pT7-FLAG-1 expression vectors (Sigma-Aldrich) to generate HA-AURKA and FLAG-AURKA, respectively, and proteins were expressed with a TNT Quick Coupled Transcription/Translation System (Promega, Madison, WI, USA) according to the manufacturer's protocol. Purified human AXIN1-MYC/DDK (TP308349) and TPX2-MYC/DDK (TP305821) proteins were obtained from OriGene Technologies (Rockville, MD, USA). GST-tagged AURORA A, Active (A28-18G) and Inactive (A28-14G) proteins were obtained from SignalChem (Richmond, Canada). Purified XMP215-His protein has been described previously[82].

In-cell fluorescence colocalization assay, immunoprecipitation, in vitro pull-down assays and cell proliferation assays

For preliminary detection of protein-protein association, target molecules were tagged with GFP (EGFP or Emerald GFP) or RFP (TagRFP-T or mApple) and overexpressed in HEK293T cells, and their colocalization analyzed under fluorescence microscopy (in-cell colocalization assay). For *in vitro* pull-down assays, proteins fused to GST were synthesized in *E. coli* and isolated by absorption to Glutathione Sepharose (GE Health Care). GST and GST-fusion proteins (2 μg)

immobilized to beads were incubated for 1 h at 4°C with *in vitro* transcription/translation products (HA-AURKA and FLAG-AURKA) or purified XMAP215-His protein in 500 μl of binding buffer (0.1% NP-40, 50 mM HEPES (pH 7.0), 150 mM NaCl, 50 mM NaF, 5 mM EDTA, 1 mM DTT, 1 μg/ml aprotinin, 1 μg/ml leupeptin, 50 μg/ml PMSF) and then washed extensively three times with binding buffer. Proteins adhering to the beads were resolved by sodium dodecyl sulfate polyacrylamide gel electrophoresis (SDS-PAGE), transferred to a polyvinylidene difluoride membrane filters (Millipore), and analyzed by immunoblotting. For the pull-down experiments, HEK293 cells were transfected with FLAG-tagged AXIN1-DIX(600-862) and extracted in lysis buffer (50 mM Tris HCl pH 7.5, 150 mM NaCl, 5 mM EDTA, 1% Triton X-100, 2 mM Na3VO4, 10 mM NaF, 1 mM DTT). Cell lysates (500 μl) were incubated with 2 μg GST or GST-APC-221-880 bound to Glutathione Sepharose beads for 1 h at 4°C. The beads were then washed three times with wash buffer (20 mM Tris HCl pH 8.0, 150 mM NaCl, 0.5% NP-40) and boiled in SDS sample loading buffer. Protein complexes were separated by SDS-PAGE and detected by immunoblotting. For cell proliferation assays, SW480 and HT29 cells expressing lentiviral-shRNA were seeded in six-well plates (1.3×10^6 cells per well and 1×10^6 cells per well, respectively) and cell proliferation was measured by counting cell number after 3 day and 4 days of incubation, respectively. Cells infected with lentivirus containing empty vector were used as controls.

In vitro kinase assay

AURKA autophosphorylation was evaluated using the ADP-Glo Kinase Assay (Promega) according to the manufacturer's instructions. The ADP-Glo Kinase Assay is a luminescent kinase assay that measures ADP formed via a kinase reaction. Briefly, inactive AURKA (0.3 pmol; SignalChem) was mixed with various concentrations (0.5-2 pmol) of purified GST, Axin1

(OriGene Technologies) or TPX2 (SignalChem) for 10 min at RT. The mixture was further incubated with 50 µM ATP in Reaction Buffer A (40 mM Tris, pH 7.5, 20 mM $MgCl_2$, 0.1 mg/ml BSA) supplemented with 50 µM dithiothreitol (DTT) in a 25 µl volume for 30 min at RT. The reaction was terminated by adding 25 µl of ADP-Glo Reagent. After incubation for 40 min at RT, 50 µL of the Kinase Detection Reagent was added and incubated for 30 min at RT. The luminescence was measured using a luminometer (Berthold Technologies, Bad Wildbad, Germany). Data from three independent experiments were averaged after normalization against the control value (AURKA only) which was set to 1.0.

Western blotting

Total cell lysates were prepared in Laemmli SDS-sample buffer supplemented with Protease Inhibitor Cocktail (Nacalai Tesque, Kyoto, Japan) and protein concentrations were quantified by the DC protein assay (Bio-Rad, CA, USA). Protein concentrations were normalized if necessary and boiled for 5 min with 2-mercaptoethanol, loaded the same amount of protein in each lane, separated by SDS-PAGE, and transferred to 0.45 µm Immobilon-P polyvinylidene fluoride membranes (Millipore). Proteins were visualized using Amersham ECL Select Western Blotting Detection Reagents (GE Healthcare) or Chemi-Lumi One Super reagent (Nacalai Tesque) and detected with a chemiluminescence imaging system Davinhc-Chemi (CoreBio, Taoyuan, Taiwan) or Amersham Imager 680 (GE Healthcare). For detection of phosphorylated proteins, cell lysates were immediately boiled for 5 min with 2-mercaptoethanol without concentration adjustment.

Fluorescence microscopy of immunostained specimens and data analysis

The immunostained specimens were observed using an LSM780 confocal microscope with a Plan-APOCHROMAT 63×/1.4 NA oil immersion objective, a Plan-APOCHROMAT 40×/1.3NA

oil immersion objective, a Plan-APOCHROMAT 10×/0.45 NA objective, four laser lines (405 nm; Multi-Ar, 458, 488, 514 nm; DPSS, 561 nm; He-Ne, 633 nm), and a highly-sensitive gallium arsenide phosphide (GaAsP) detector (Carl Zeiss) and an LSM880 confocal microscope with a Plan-APOCHROMAT 63×/1.4 NA oil immersion for SR objective, a Plan-APOCHROMAT 40×/1.3 NA oil immersion for SR objective, a Plan-APOCHROMAT 10×/0.45 NA objective, four laser lines (405 nm; Multi-Ar, 458, 488, 514 nm; DPSS, 561 nm; He-Ne, 633 nm), and a GaAsP detector (Carl Zeiss). Detection and quantitative analysis of phosphorylated proteins were performed using cultured cells and paraffin-embedded tissues fixed in 4% paraformaldehyde or formalin, respectively. To compare immunostaining intensities in each cell type cultured on different cover slips, the cover slips were processed under the same conditions and intensity values were obtained as relative values against that of control cells, which was set to 1. To compare immunostaining intensities in different tissue sections, the sections were bound to a single slide glass to be processed under the same staining conditions. For tumour cells analysis in the intestinal tissue specimens, tumour cells in each polyp were specified by their epithelial features shown with E-cadherin or β-catenin immunostaining.

To define the percentage of cells with γH2A.X-positive micronuclei in mouse tumours, cells with γH2A.X-positive micronuclei were counted in normal crypts and each polyp throughout the entire Swiss roll section, and the total numbers were divided by the estimated total numbers of cells in total crypt in the section and in each polyp obtained from cell densities and areas, respectively. Estimated total cell numbers were 100000 for crypt, 34338 for total tumours analyzed. Sample sizes indicate the numbers of images analysed. To measure fluorescence on centrosomes, maximum intensity projections of z-stack images were produced, and centrosomal regions were manually selected to obtain total fluorescence values in the region

of interest using the ImageJ software. The average fluorescence intensities and phospho-to-total protein intensities were normalized to those of controls, which were defined as 1.0. For mouse intestines, average values from crypt cells were used as standards. For β-catenin- and TPX2-labeling in mouse intestine, values from crypt cells in the neighbourhood of the polyps along the intestinal tract were used as standards. For human tumours, the average values in polyp#2 were normalized to those of polyp#1 without APC mutation. Sample sizes indicate the numbers of cells (β-catenin)/centrosomes (AURKA)/spindles (TPX2) analysed. To define the percentage of Ki67-positive cells in AURKA inhibitor–treated mouse tumors, paraffin-embedded tissues fixed in formalin were stained for β-catenin, Ki67, and nuclear DNA (with Hoechst 33342), imaged on a confocal microscope, and analysed using the MetaMorph software. The Ki67- and Hoechst 33342–positive areas were determined by intensity thresholding in the crypts and tumor tissues, and the percentage of Ki67-positive areas were calculated in each image obtained from multiple crypt/tumor areas. Sample sizes indicate the numbers of images analysed. To count mitotic cells in mouse intestines, the tissue sections were stained with Hoechst33342 and imaged using an Imager Z1 fluorescence microscope (Carl Zeiss), and total and mitotic cells were manually counted based on the shapes of chromosomes.

Live imaging and data analysis

Time-lapse phase-contrast live imaging of cells was performed using an IX81-ZDC inverted microscope with a 20× objective lens LUCPLFN 20×PH (Olympus) controlled by MetaMorph software (Molecular Devices, Sunnyvale, CA, USA). The microscope was installed in a temperature-controlled dark box and was equipped with a motorized XYZ stage, a ZDC (Z drift compensator) autofocus system, a cooled CCD camera ORCA-AG (Hamamatsu Photonics, Shizuoka, Japan), and a heat controller (Tokai Hit, Shizuoka, Japan) and gas mixer

(Olympus/Tokken, Chiba, Japan) for cell culture. During imaging cells were maintained at 37°C in a 5% CO_2 atmosphere. Duration of mitosis and doubling time were manually measured. Time-lapse images were edited using ImageJ and QuickTime Pro software (Apple). Fluorescence recovery after photobleaching (FRAP) analysis of GFP-AURKA-expressing cells was performed using a DeltaVision system and Photokinetics data analysis software (GE Healthcare, Pittsburgh, PA, USA). A centrosomal area of approximately 3 μm diameter was bleached using a 488 nm Quantifiable Laser Module while collecting time-lapse images at 1 s intervals.

Animals and human colorectal adenoma

Animals were used in accordance with governmental and institutional regulations and protocols were approved by the Animal Care and Use Committee of the RIKEN Kobe Institute, Kanazawa University and the University of Tokyo. All animals were cared for in accordance with the ethical standards of the institutions. *Apc*$^{\Delta 716}$ mice and paraffin-embedded tissue preparation were described previously[83]. *Apc*^{1638T} mice (backcrossed to C57BL/6) were described previously[39, 84]. Wild-type C57BL/6J mice were purchased from Charles River Laboratories Japan Inc. (Kanagawa, Japan). For AURKA inhibitor treatment, wild-type and *Apc*$^{\Delta 716}$ mice were dosed orally twice daily for 14 consecutive days for Ki67 staining (two mice in each group) and 28 consecutive days for polyp number counting (ten mice in each group), with vehicle, 20 mg/kg alisertib (CS-0106, Chemscene LLC, Monmouth Junction, NJ, USA), or 30 mg/kg MLN8054 (CS-0010, Chemscene LLC) as a solution in 10% 2-HP-β-CD[85]. For polyp counts, incised intestinal tracts were briefly stained in 0.1% methylene blue, and counted under a dissecting microscope and were categorized according to size (<2 , 2–3 and >3 mm). Human colorectal polyps were excised by polypectomy at the Nico-tama Coloproctology Clinic with informed consent and the protocol was approved by the Ethical Committee of the Riken Kobe Institute.

Samples were de-identified and analyzed anonymously. A small portion of the polyp was used for genomic DNA isolation using a DNeasy Blood & Tissue Kit (Qiagen, Hilden, Germany), and the remaining portion was immediately fixed in formalin and embedded in paraffin. For genomic sequencing, the last exon of *APC*, encoding from the armadillo repeat region to the stop codon, was cloned by PCR as a fragment of 1000~1700 bp using specific primers, inserted into pCR-Blunt II-TOPO (Thermo Fisher Scientific, Waltham, MA, USA) and analyzed by Sanger sequencing. In this study, a hyperplasia polyp without APC mutation (polyp#1, Asian female, early 60s) and a low-grade tubular adenoma with two truncating mutations (c.2698G>T and c4558G del) (polyp#2, Asian female, late 50s) were used. Images of hematoxylin-eosin (HE) stained sections of a formalin-fixed, paraffin-embedded Swiss roll of the intestine of an $Apc^{\Delta 716}$ mouse and of human polyps were collected using a SZX12 stereomicroscope with a DF PLAPO 1.2× PF2 objective (Olympus, Tokyo, Japan) or a Primo Vert Monitor with a Plan-ACHROMAT 4×/0.10 NA objective (Carl Zeiss, Jena, Germany), respectively.

Comparative genomic hybridization (CGH) microarray analysis

CGH microarray analysis was performed by Takara Bio using a SurePrint G3 Mouse CGH Microarray Kit, 1×1M (Agilent Technologies, CA, USA). The genomic DNAs from $APC^{\Delta 716}$ mouse normal intestines (control) and polyps were fragmented, amplified, and then labelled with Cy3 or Cy5 dyes. Dye-swap replication experiments were performed for each polyp sample vs. control DNA. The hybridized DNAs were applied to the microarray and scanned on an Agilent SureScan Microarray Scanner. The results were analysed using the Agilent Genomic Workbench 7.0 software (Agilent Technologies); experimental parameters were set with consideration for the mosaicism of mutations in the tumour cells and the presence of a considerable amount of normal cells in each sample. For pre-processing: Feature Filter, ON; Design Filter, v2; GC correction,

ON; Centralization, ON; Intra array, ON. For Aberration Filter: $Log_2Ratio \geqq 0.01$; minimum number of probes in region, 5. For analysis, the AMD-2 algorithm with threshold 6 was used. Array CGH profiles derived from two dye-swap experiments were plotted together on the same plot. Synteny between human and mouse chromosomes were analysed on the Ensembl Comparative Genomics/Synteny website. The ideograms of human chromosomes 13 and 20 and mouse chromosomes 2 and 14 shown in Fig. 5e were generated by tracing illustrations in the Ideogram View on the NCBI Genome Data Viewer website. Syntenic comparison of human and mouse chromosome was performed using Comparative Genomics/Synteny tool on Ensembl website.

Genomic DNA isolation and quantitative PCR (qPCR)

Genomic DNA was extracted from mouse tissues using ISOGENOME (Nippon Gene, Tokyo, Japan) in accordance with the manufacturer's instructions. Five nanograms of genomic DNA was applied to qPCR using PowerUp SYBR Green Master Mix (Applied Biosystems, Foster City, CA, USA) and the QuantStudio 5 Real-time PCR System (Applied Biosystems). The reaction was first incubated at 50°C for 2 min and then at 95°C for 2 min, followed by 40 cycles at 95°C for 15 sec and 60°C for 1 min. *Zfp438* located on mouse chromosome 18A1 was used as the internal reference gene for qPCR because our CGH microarray analysis did not show the presence of genetic alterations in the A1–A2 region of chromosome 18 in intestinal polyps of $Apc^{\Delta 716}$ mice. The results were normalized to the values obtained for *Zfp438* and analysed by the $2^{-\Delta\Delta CT}$ method. For qPCR of human samples, *SMG1* was used as the internal reference gene because copy number alterations of chromosome 16p12.3 that harbours the *SMG1* gene have not been observed in colorectal cancers[86]. Human normal genomic DNA was obtained from Promega (Madison, WI, USA) and the values are averages of three replicates. The primer

sequences were as follows: m*Aurka* 5′-TGGCTCAAACGGAGAGTTGA-3′ and 5′-CCTGGAATCCCATACCTGGA-3′; m*Bora*, 5′-TAGGTTGGACGGTCCCTCAC-3′ and 5′-GCAGCACAGACATGGAGAGC-3′; m*Tpx2*, 5′-GCATGCGTTTTGTTCCTCTG-3′ and 5′-GCTGCATGATCCCAATGCTA-3′; m*Zfp438*, 5′-GGCTGTTGCTGTGCTGTACC-3′ and 5′-CTCCCTGGGCCATCAGTAAG-3′; h*AURKA*, 5′-GGGCAATGGATTTCACTCCT-3′ and 5′-GGTGTGGAGGAAGTGGCAGT-3′; h*BORA*, 5′-TTGCATCCTCCAGTGGTCCT-3′ and 5′-GCTGCATTGAAAAGGGCTTG-3′; h*TPX2*, 5′-AATCACCGTCCCCAAGTCAC-3′ and 5′-TCCCAGGGAATCACCTCATC-3′; and h*SMG1*, 5′- AAACTTTGCTTTCGGCACCA-3′ and 5′-CAAGCCCTCGGACTCACACT-3′.

Mutation and copy number analyses using TCGA data

Exome and SNP array data from The Cancer Genome Atlas (TCGA)-colon adenocarcinomas (COAD) and rectum adenocarcinomas (READ) paired tumour/normal samples were prepared as described previously[87] Briefly, mutation calling from the exome data was performed using the *EBCall* algorithm[88] and absolute copy number profiles were obtained from the SNP array data using the ASCAT algorithm[89]. We analysed the copy numbers of 13q and 20q. For 20q, the *AURKA* locus alone, *TPX2* locus alone, and 20q that contained both loci were analysed independently. We assumed that 13q, 20q, AURKA, or TPX2 had undergone chromosomal gain if the sum of the allele-specific copy numbers averaged along the loci was greater than or equal to three. Similarly, each locus was assumed to have undergone chromosomal loss if the total copy number was less than or equal to one. For the *APC* mutation, we analysed only patient samples with *APC* truncations within the region between the N-terminus SAMP repeats. Seven cases with β-catenin-stabilizing mutations were omitted from the analysis. In total, 291 COAD and 111 READ TCGA patient samples were selected. The 402 patient samples were divided into

three groups as follows. Class 1: Lesions without a truncating mutation and LOH in the *APC* locus; Class 2: Lesions with one truncating mutation or one LOH in the *APC* locus, which are expected to have a single *APC* mutation and retain a single wildtype copy of *APC*; Class 3: Lesions with two or more (two to three as a result) truncating mutations in the *APC* locus, or one or more (one to three as a result) truncating mutations, and LOH in the *APC* locus, which are expected to have no wildtype *APC*.

Among the three groups, copy number alterations of 13q, 20q, *AURKA*, and *TPX2* were analysed by the chi-squared test (two sided) and Mann–Whitney *U*-test (two sided). Because the results for 20q, *AURKA*, and *TPX2* were almost the same, only 20q results are presented.

The microsatellite instable (MSI) status and clinicopathological parameters of all COAD and READ patient samples were also obtained from TCGA database. The samples were divided into two subgroups, microsatellite stable (MSS) and microsatellite instable (MSI) in accordance with the MSI status and then the presence or absence of an *APC* mutation was compared between each subgroup. The distant metastasis status and number of regional lymph node metastases were compared between samples with copy number gain of 13q or 20q and samples with a normal copy number. These data were analysed by Fisher's exact test.

Karyotyping of chromosomes in MCF10A and APC883 cells

The APC833 cell line was generated from the MCF10A cell line, a genetically stable human mammary gland epithelial cell line[90], by introducing a truncation mutation into the APC locus by genome editing. The MCF10A cell line was established in 1990 from human fibrocystic mammary tissue[91]. Karyotyping prior to immortalization showed normal diploidy, but later passages showed near-diploidy with some rearrangements interpreted as 48,XX,3p-,6p+,8+,9p+,16+, including a balanced reciprocal translocation t(3;9)(p13;p22) and an

unbalanced translocation t(5q;der[9])[91] In later studies, gain at chromosome 1q was reported[92, 93], as observed in this study. Trisomy 20 is recurrent in subsequent studies[92, 93, 94, 95],

In this study, Q-banding (20 cells for each cell type) were performed by Chromosome Science Labo (Hokkaido, Japan). Complete description of karyotyping results is shown in Extended Data Table 3. In our early analysis, detailed rearrangement of one chromosome 8 was not determined and was described as "dup8(p?)" In later analysis, the structure of the rearranged chromosome 8 was analyzed by FISH using specific probes (8p11, 8p23, 8q13, 8q21, 8q24) and the description was updated to "der(8)dup(8)(q22q24.3)ins(8)(p24.3q22q24.3)". For the transformed, near-tetraploid APC883 cells, common number imbalances are shown by letter color for karyotype description: cyan, three chromosome 6s; brown, five chromosome 8s; red, six chromosome 20s (Extended Data Table 3), and by box color for chromosome images: cyan, three chromosome 6s; brown, five chromosome 8s; red, six chromosome 20s. To analyze newly generated chromosome aberrations, types of abnormalities were classified as tetraploidy, gain, loss, deletion and fusion. The fusion includes all types of chromosomes generated by fusions such as translocation, robertsonian translocation and telomere association. To separate subclones MCF10A cells carrying chromosome 20 disomy [MCF10A(20di)] and trisomy [MCF10A(20tri)], clones were isolated by colony picking followed by Q-banding to determine karyotype.

Statistics and reproducibility

Statistical evaluation was carried out by the Student's t-test (two sided), chi-squared test (two sided), Tukey–Kramer method (two sided), F-test (two sided), or Mann–Whitney U-test (two sided) as indicated. P-values and sample size are shown in each figure. Biochemical experiments were repeated with at least three independent preparations with similar results. For quantification

of image data to ensure adequate power to detect significance, sufficient numbers of regions/cells were analysed as indicated in each figure.

Data availability

Data are available on request from the authors. Materials used in this study are available for distribution after an MTA, except for materials from human research participants. The aCGH data have been deposited in the NCBI Gene Expression Omnibus (GEO; http://www.ncbi.nlm.nih.gov/geo/) and are accessible through GEO series accession number GSE3642. accession GSE63306 (https://www.ncbi.nlm.nih.gov/geo/query/acc.cgi?acc= GSE63306).

Code availability

Computer codes are available on request from the authors. The code to create the 2D rotational projection of EB1 comet data has been deposited in Github (https://github.com/wxchew/cometdensity/blob/master/2DProjectedCometDensity.ipynb).

Acknowledgements

We are grateful to Dr. Atsushi Ochiai (NCC-EPOC) for his guidance on tumor analysis, and Yuki Tano (Riken BDR) for her assistance in experiments and data processing. We are grateful also to Dr. Yoshinobu Uno (Riken BDR) for his instruction of FISH analysis, Drs. Akira Nagafuchi (Nara Medical Univ), Takashi Toda (Hiroshima Univ), Kazuo Yamagata (Kindai Univ), Mika Toya (Waseda Univ), Tomoya Kitajima (Riken BDR), Masatoshi Takeichi (Riken BDR), Chikara Furusawa (Univ. of Tokyo), Shigeru Kuratani (Riken BDR), and Yoshimi Takai (Kobe Univ) for critical reading of the manuscript and valuable suggestions. Our special thanks

are also due to Ms. Masaki Yamaguchi amd Mr. Yasuhiko Sato (Carl Zeiss Japan), Mr. Mitsunari Yamaguchi (Molecular Devices Japan), and Mrs. Yuichiro Imai and Masashi Emi (Olympus) for excellent technical assistance in operating the microscope systems and image analysis software. Y.M.-K. was supported by the Japan Society for the Promotion of Science–NEXT program (LS128), the Takeda Science Foundation, the Uehara Memorial Foundation, a Grant-in-Aid for Challenging Exploratory Research (Japan Society for the Promotion of Science KAKENHI no. 20K20379), and Japan Science and Technology Agency Core Research for Evolutional Science and Technology (no. JPMJCR1863), Extramural Collaborative Research Grant of Cancer Research Institute, Kanazawa University, and an intramural grant from RIKEN. The results published here are in part based upon data generated by the TCGA Research Network: http://cancergenome.nih.gov/. Imaging experiments were in part supported by the RIKEN Kobe Light Microscopy Facility. Animal experiments were in part supported by the Laboratory for Animal Resources and Genetic Engineering at the RIKEN BDR.

Author contributions

Y.K., T.H., K.O., A.H. and T.N. performed experiments and edited the manuscript. Y.W., M.O., S.S., and N.T. performed experiments. Y.K., A.N., and K.M. analyzed TCGA data using informatics techniques. T.K., T.S., M.O., K.F., A.K., P.O W. and H.O. prepared biological samples. K.K. performed image data analysis and statistical data analysis. N.Y., M.M., H.Y., C.W.X., S.A., K.T., W.R.L., B-C.C. and E.B. performed imaging experiments, image processing and data analysis. R.S. and R.F. prepared biological samples and edited the manuscript. M.O., M.M.T and T.A gave conceptual and technical advices. Y.M.-K. conceived and managed the project, performed experiments, and wrote the manuscript.

Additional information

Supplementary Information accompanies this paper:

- **Supplementary Information**

  This file contains Extended Data Figure 1~8 and references.

- **Extended Data Table 1**

  This table contains representative images used in the analysis, which can be presented in the main body.

- **Extended Data Table 2**

  This table contains uncropped versions of all gels and blots.

- **Extended Data Table 3**

  This table contains full descriptions of the karyotypes of cell lines MCF10A and APC883, their subclones, and transfectants. Newly generated chromosomes, which included truncation and chromosome rearrangements, such as translocation, duplication, and telomere association, are shown in bold. For transformed, near tetraploid APC883 cells, the common number imbalance of chromosomes 6, 8, and 20 is indicated by colour codes identical to the box colours in Extended Data Fig. 5f: cyan, three chromosome 6s; brown, five chromosome 8s; red, six chromosome 20s.

- **Movie 1**

  Three-dimensional timelapse images of a mitotic HeLa cell that expressed EB1-GFP and H2B-TagRFP collected by lattice light sheet microscopy at 10-s intervals are represented in a three-dimensional space. Time scale: h.m.s.

- **Movie 2**

Three-dimensional timelapse images of an APC-depleted mitotic HeLa cell that expressed EB1-GFP and H2B-TagRFP collected by lattice light sheet microscopy at 10-s intervals are represented in a three-dimensional space. Time scale: h.m.s.

- **Movie 3**

  Three-dimensional timelapse images of control and APC-depleted mitotic HeLa cells shown in Movies 1 and 2 were projected onto a 2D plane and combined for comparison. Time scale: h.m.s.

- **Movie 4**

  Representative phase contrast timelapse videos of MCF10A, APC883, APC883+AURKA(T288D), and APC883+β-catenin KD#1 (shRNA#1) cells. Timelapse images at 10-min intervals for 64 h are displayed from videos that recorded at 5-min intervals. Time scale: h:m:s.ms.

- **Movie 5**

  Representative phase contrast timelapse videos of MCF10A, APC883, and transformed (near tetraploid) APC883 cells that spontaneously appeared after >5 months of passaging, and APC883+TPX2 cells. Timelapse images at 10-min intervals for 64 h are displayed from videos that recorded at 5-min intervals. MCF10A and APC883 videos are the same as those shown in Movie 4 for comparison. Time scale: h:m:s.ms.

- **Movie 6**

  Representative phase contrast timelapse videos of MCF10A, APC883, MCF10A+MMβ-catenin, and APC883+β-catenin KD#2 (shRNA#2) cells. Timelapse images at 10-min intervals for 64 h are displayed from videos that recorded at 5-min intervals. MCF10A and

APC883 videos are the same as those shown in Movie 4 for comparison. Time scale: h:m:s.ms.

- **Movie 7**

  Representative phase contrast timelapse videos of MCF10A(20di), MCF10A(20di) + APC shRNA, MCF10A(20tri), and MCF10A(20tri) + APC shRNA cells. Timelapse images at 10-min intervals for 64 h are displayed from videos that recorded at 5-min intervals. Time scale: h:m:s.ms.

Competing interests: Portions of the technology described herein are covered by U.S. Patent 7,894,136 issued to Eric Betzig (EB) and assigned to Lattice Light, LLC of Ashburn, VA, U.S. Patents 8,711,211 and 9,477,074 issued to EB and assigned to HHMI, U.S. Patent application 13/844,405 filed by EB and Kai Wang (KW) and assigned to HHMI, and U.S. Patent 9,500,846 issued to EB and KW and assigned to HHMI.

Extended Data Figure 1 Kawasaki et al.

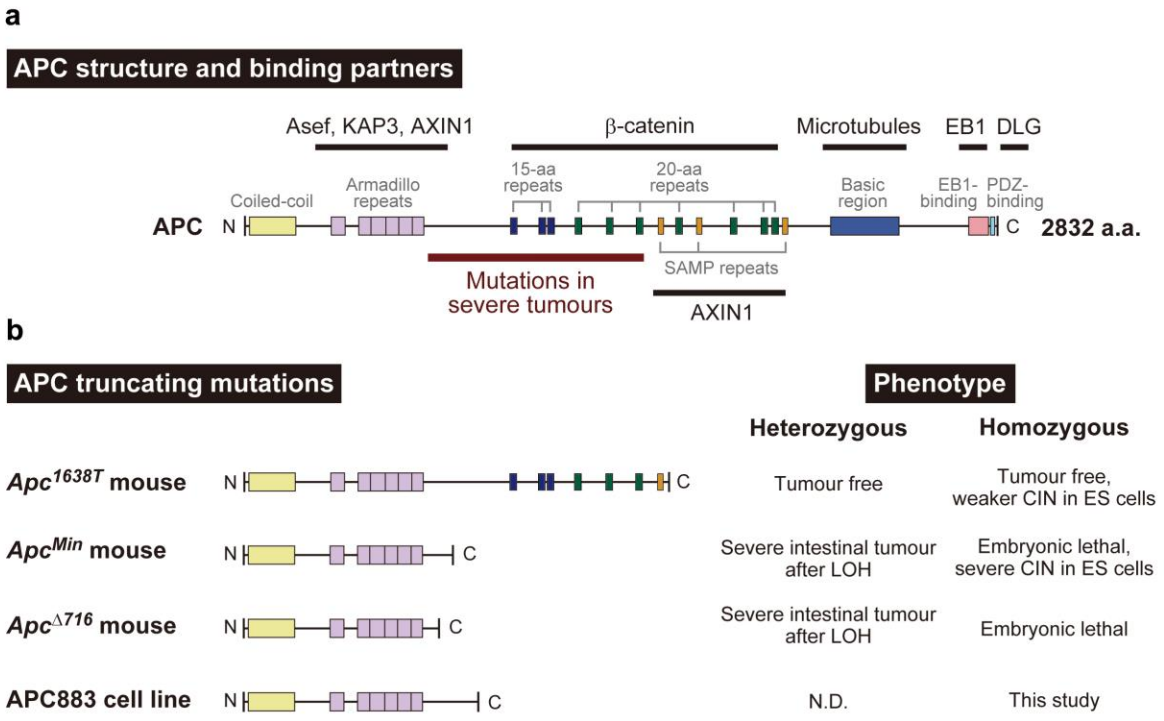

Extended Data Fig. 1 | APC structure and phenotypes. (**a**) Domain structures of full-length APC and major binding partners[1, 2, 3, 4, 5, 6, 7]. The *APC* gene is responsible for many sporadic cases of gastrointestinal cancers and familial adenomatous polyposis, a dominantly inherited colorectal tumour predisposition that results from germline mutations in APC[8, 9, 10, 11, 12, 13, 14]. Tumours start developing upon mutation in both alleles. In general, *APC* mutations that result in stable proteins truncated in the region between the armadillo repeat and first SAMP motif are associated with severe polyposis phenotypes (reviewed in 4, 15). (**b**) Truncated *APC* mutants. Phenotypes of cells and mice are shown on the right. Heterozygous *Apc* mutations, such as Apc^{Min} and $Apc^{\Delta 716}$, lead to severe polyposis after loss of the wildtype allele (>~30 polyps), whereas their homozygosity results in embryonic lethality[16, 17, 18]. Homozygous Apc^{1638T} mice with a truncating mutation just after the first SAMP motif, which retains the β-catenin

destruction ability, are viable and do not develop any tumours, thereby demonstrating that this N-terminal fragment that retains the first SAMP motif is sufficient for the tumour-suppressing function[19]. Nevertheless, *Apc*^{1638T} homozygous ES cells have a CIN phenotype, although it is weaker than that in *Apc*^{Min} homozygous ES cells[20]. MCF10A-derived cell line APC883 with a homozygous APC truncation was generated by genome editing.

Extended Data Figure 2 Kawasaki et al.

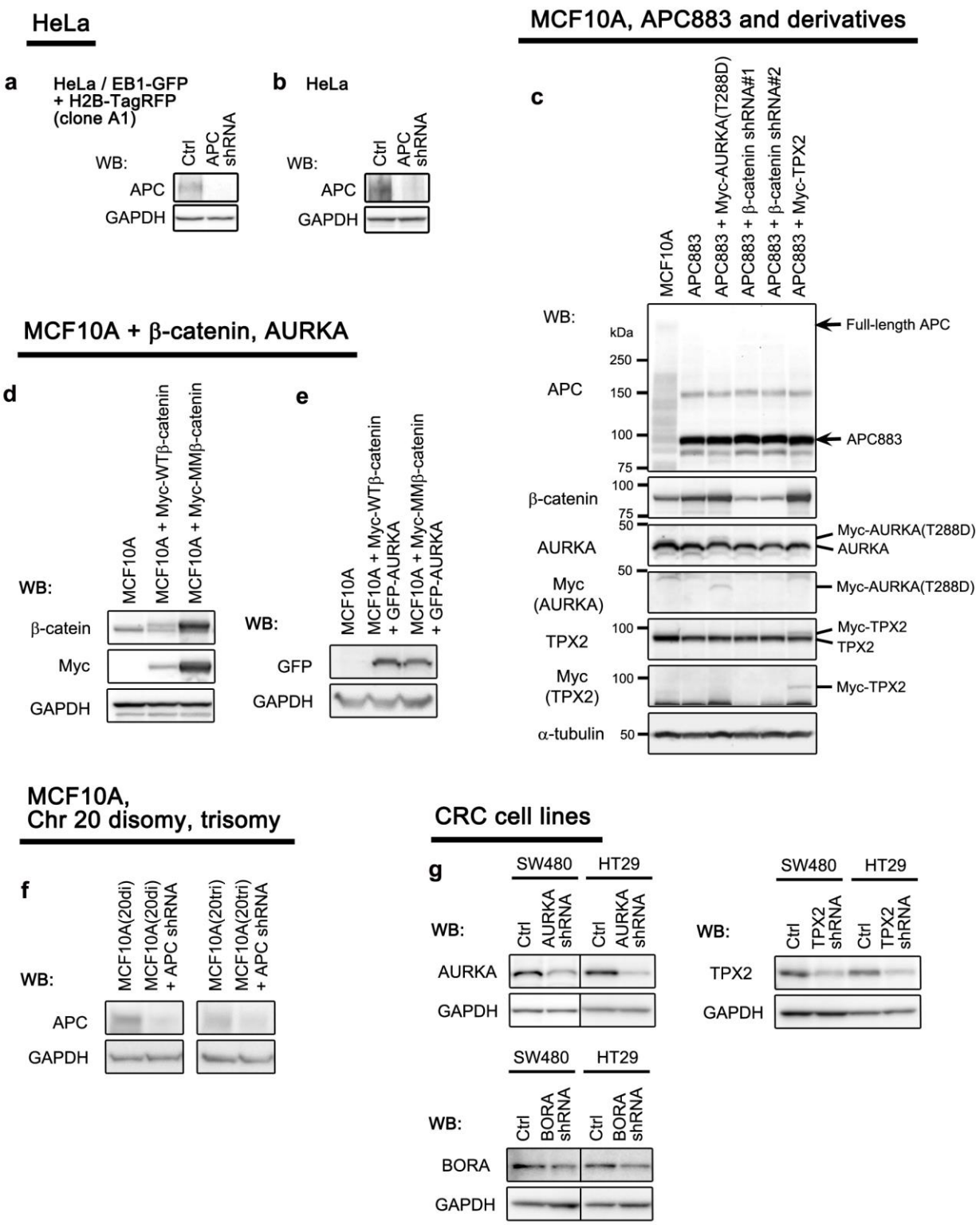

Extended Data Fig. 2 | Characterization of cells used in this study. (**a, b**) Western blot analysis of HeLa cells and HeLa cells that expressed EB1-GFP and H2B-TagRFP (clone A1)[21] before and after constitutive transfection with shRNA against APC (APC KD). APC knockdown efficiency was ~70%. (**c**) Characterization of MCF10A cells, APC883 cells, and APC883 cell-derived transfectants. Cell lysates were subjected to western blot analysis using the indicated antibodies. Full-length APC and truncated APC883 protein are indicated. For Myc-AURKA (T288D) and Myc-TPX2, endogenous and exogenous Myc-tagged proteins are indicated. (**d, e**) Characterization of MCF10A cells transfected with Myc-tagged wildtype β-catenin (Myc-WTβ-catenin) and a dominant stable β-catenin (Myc-MMβ-catenin), and further transfected with GFP-AURKA for fluorescence recovery after photobleaching (FRAP) analysis. Myc-WTβ-catenin- and Myc-MMβ-catenin-transfected cells were established under the same conditions, but Myc-WTβ-catenin was hardly overexpressed. (**f**) MCF10A subclones with chromosome 20 disomy or trisomy and transfected with APC shRNA. (**g**) CRC cell lines SW480 and HT29 were transfected with shRNAs against AURKA, TPX2, or BORA. See also Extended Data Table 2.

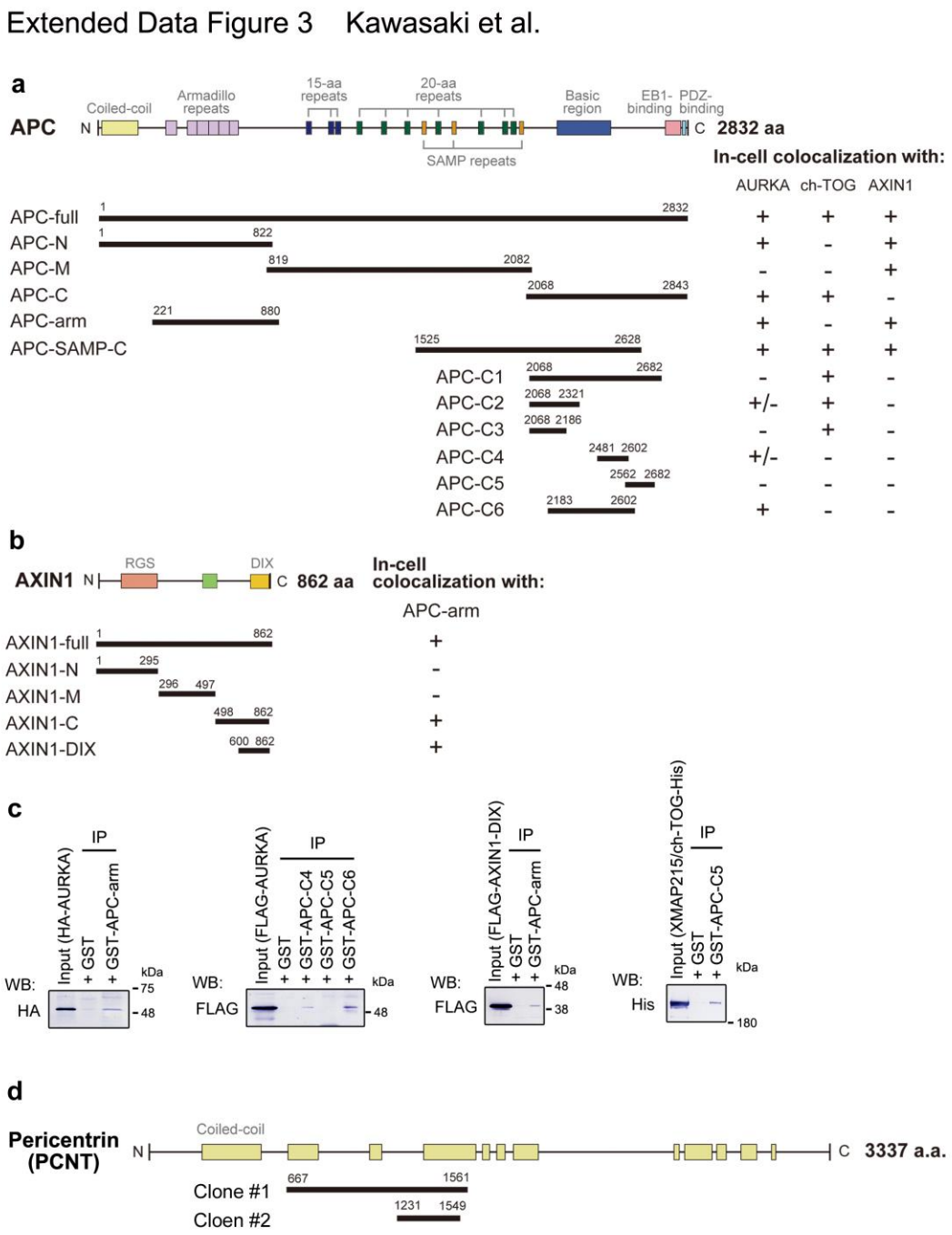

Extended Data Fig. 3 | Identification of APC-binding proteins. (**a, b**) Domain structures of APC and AXIN1, and the analysed fragments. Amino acid numbering is based on human APC transcript variant 3 (NM_000038) and human AXIN1 transcript variant 1 (NM_003502).

Associations of APC with AURKA and AXIN1 were assessed by in-cell colocalization analysis using a series of deletion mutants. The results are shown on the right. (**c**) Direct binding between APC fragments and AURKA/AXIN1/ch-TOG predicted in (a) was confirmed by in vitro pull-down assays using purified proteins. The APC arm and APC-C6 bound to AURKA. The APC arm also bound to the C-terminal DIX domain of AXIN1. XMAP215[22], the Xenopus homologue of ch-TOG, bound to APC-C3. We used Xenopus XMAP215 because we could not purify full-length human ch-TOG from *E. coli*. The C-terminal one-third bound to the APC arm. See also Extended Data Table 2. (**d**) Yeast two-hybrid screening using the APC arm region as bait identified pericentrin. The two identified pericentrin clones are shown.

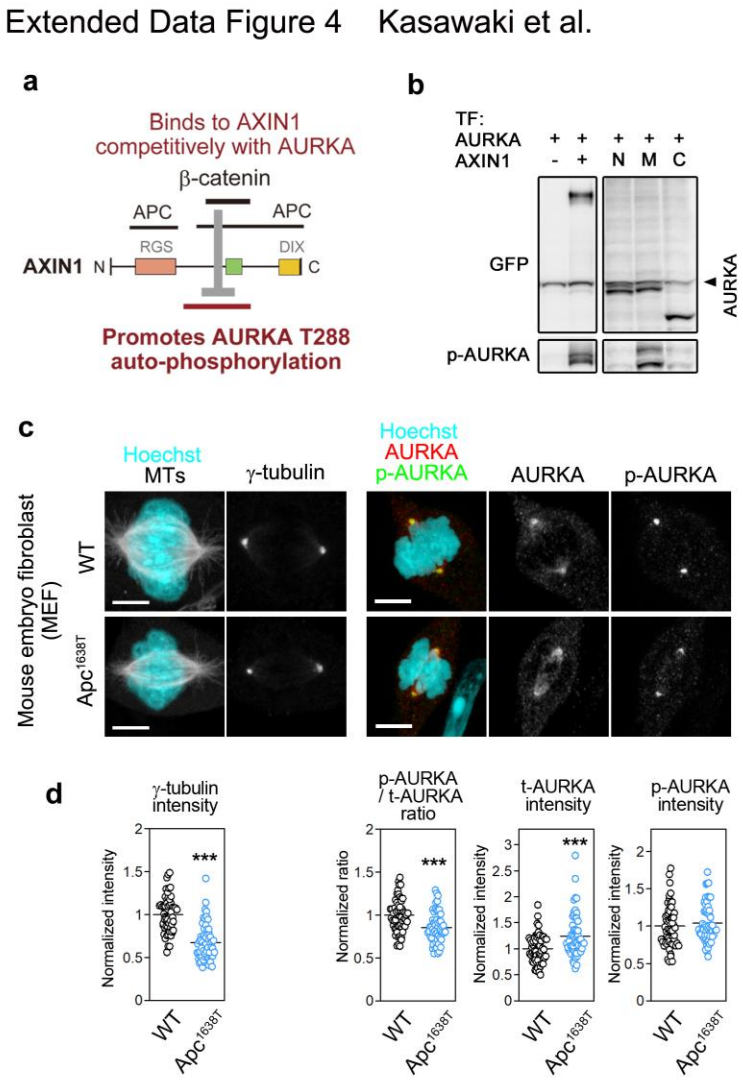

Extended Data Fig. 4 | Biochemical analysis of AURKA regulation by APC and AXIN1. (**a**) AXIN1 structure and AURKA-activating region that also binds to β-catenin[23]. (**b**) Effects of AXIN1 on AURKA phosphorylation were analysed using the HEK293T cell overexpression assay system. HEK293T cells were transfected with GFP-fused AURKA and full-length AXIN1 or fragments, lysed, and then subjected to western blot analysis using anti-GFP and anti-p-T288 AURKA antibodies. The left panel is same with Fig. 2e. See also Extended Data Table 2. (**c, d**) Analysis of primary MEFs from wildtype (WT) and *Apc*^{1638T} mice. Immunostaining of microtubules (MTs), γ-tubulin, AURKA, and p-T288 AURKA (c). Immunostaining intensity of

γ-tubulin, total AURKA protein levels (t-AURKA), autophosphorylated AURKA levels (p-AURKA), and the autophosphorylation ratio (p-AURKA/t-AURKA ratio) were normalized to those of the wildtype, which were set to 1.0 (d). Scale bars: 5 μm. ***$P < 0.001$; Student's t-test.

Extended Data Figure 5 Kawasaki et al.

a MCF10A

Type No.1: Chromosome 20 trisomy

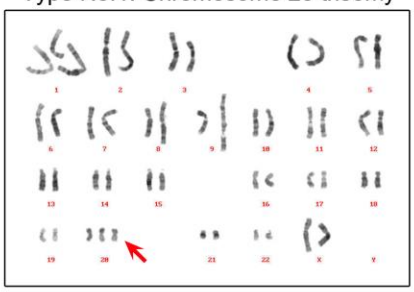

Type No.2: Chromosome 20 disomy

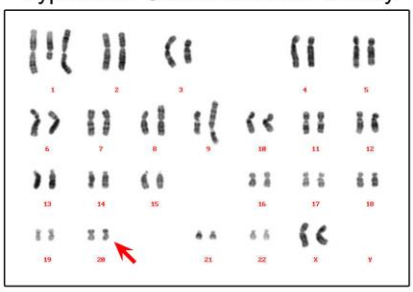

c APC883 + β-catenin shRNA#1

Type No.1: Original karyotype

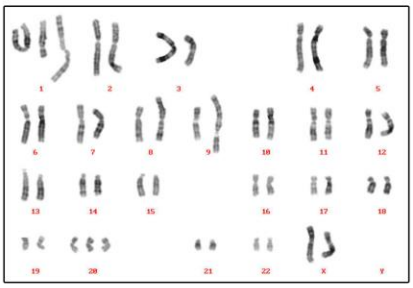

b APC883

Type No.3: Dicentric derivative chromosome containing chrmosome 7 and 9

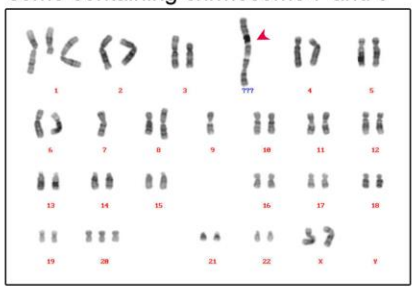

Type No.5: Derivative chromosomes containing chromorome 1, and 6 and 14

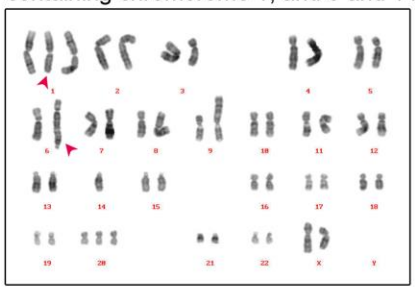

d APC883 + AURKA(T288D)

Type No.1: Original karyotype

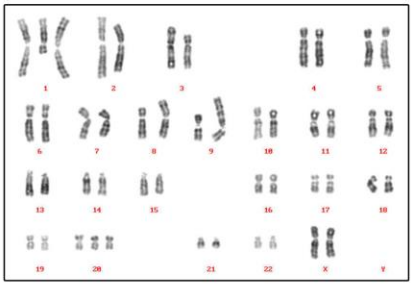

e APC883 + TPX2

Type No.3: Additional material of unknown origin on chromosome 8

Type No.5: Deletion of chromosome 1 and 12, and 1;12 translocation

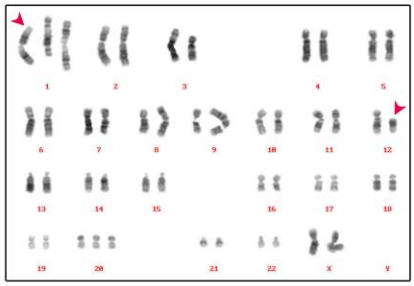

f Transformed APC883

Type No.1: Near-tetraploid

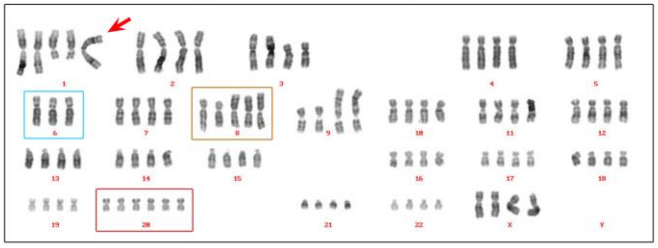

Type No.2: Near-tetraploid

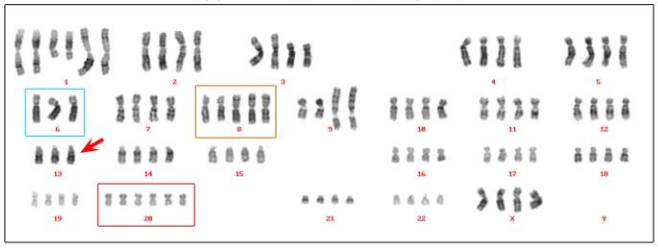

Extended Data Fig. 5 | Karyotypes of MCF10A and APC883 cells. Representative karyotype images of each cell line (20 cells were analysed in each cell line). For complete karyotype descriptions of all analysed cells, see Extended Data Table 3. The karyotypes were determined by Q-banding with Hoechst/quinacrine staining. Note that commonly observed abnormalities in chromosome 1 (deletion and partial duplication), chromosome 3 (deletion and translocation), chromosome 8 (duplication), and chromosome 9 (translocation) have been observed previously[24, 25]. (**a**) Karyotype of parental MCF10A cells that expressed full-length APC. The MCF10A cell line has two major populations with or without chromosome 20 trisomy (types 1 and 2, respectively), whereas all 20 cells showed near diploidy. Chromosome 20 is indicated by red arrows. (**b**–**f**) Karyotypes of APC883 cells and APC883-derived cells. Major karyotypes in each cell type (c, d) and representative examples with chromosome aberrations (b, e, and f) are shown. Newly derived abnormal chromosomes are indicated by red arrowheads. After reduction of β-catenin levels (c) or expression of constitutively active AURKA (T288D) (d), APC883 cells maintained their original karyotype. In TPX2-expressing APC883 cells (e), various aberrations were observed. In (f), representative karyotypes of APC883 cells after >5 months of passaging are shown. In this transformed subpopulation, all analysed cells had a near tetraploid karyotype with some numerical imbalances. Common numerical imbalances are shown by the letter colour for the karyotype description: cyan, three chromosome 6s; brown, five chromosome 8s; red, six chromosome 20s. Examples of randomly occurring imbalances are indicated by arrows.

Extended Data Figure 6 Kawasaki et al.

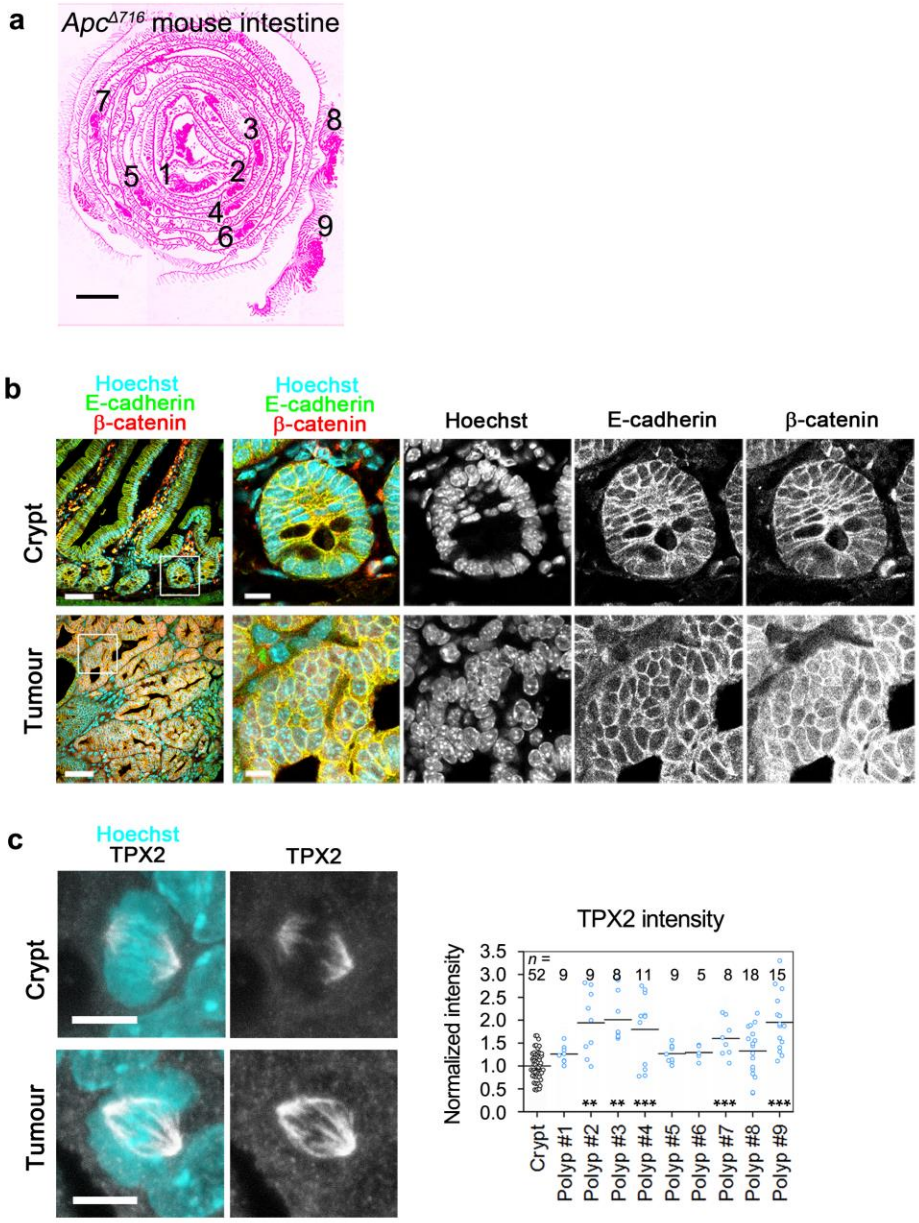

Extended Data Fig. 6 | Immunofluorescence analysis of paraffin-embedded sections of APC mutant mouse intestines. (**a**) HE-stained section of intestines from a 16-week-old *Apc*$^{\Delta 716}$ mouse. Polyps analysed in this study are indicated by numbers. (**b**) Immunostaining of a formalin-fixed, paraffin-embedded *Apc*$^{\Delta 716}$ mouse intestine section for E-cadherin and β-catenin

with nuclear DNA stained by Hoechst 33342 to visualize crypt cells (top) and tumour cells (bottom). Low magnification images are shown on the left and magnified images of the boxed areas are shown in the four panels on the right. Note that β-catenin was upregulated, but its preferential accumulation in the nucleus was not observed. (c) Upregulation of TPX2 in *Apc*$^{\Delta 716}$ tumour tissues. Immunostaining of a paraffin-embedded section for TPX2 with nuclear DNA stained by Hoechst 33342 is shown. Crypt cells (top) and tumour cells (bottom) were observed. Quantitative analysis of immunofluorescence signals of TPX2 in crypts and tumour tissues of nine polyps is shown on the right. Scale bars: 50 μm (b, low magnification, left), 10 μm (b, high magnification, right), and 5 μm (c). **$P < 0.01$; ***$P < 0.001$; Tukey–Kramer test.

Extended Data Figure 7 Kawasaki et al.

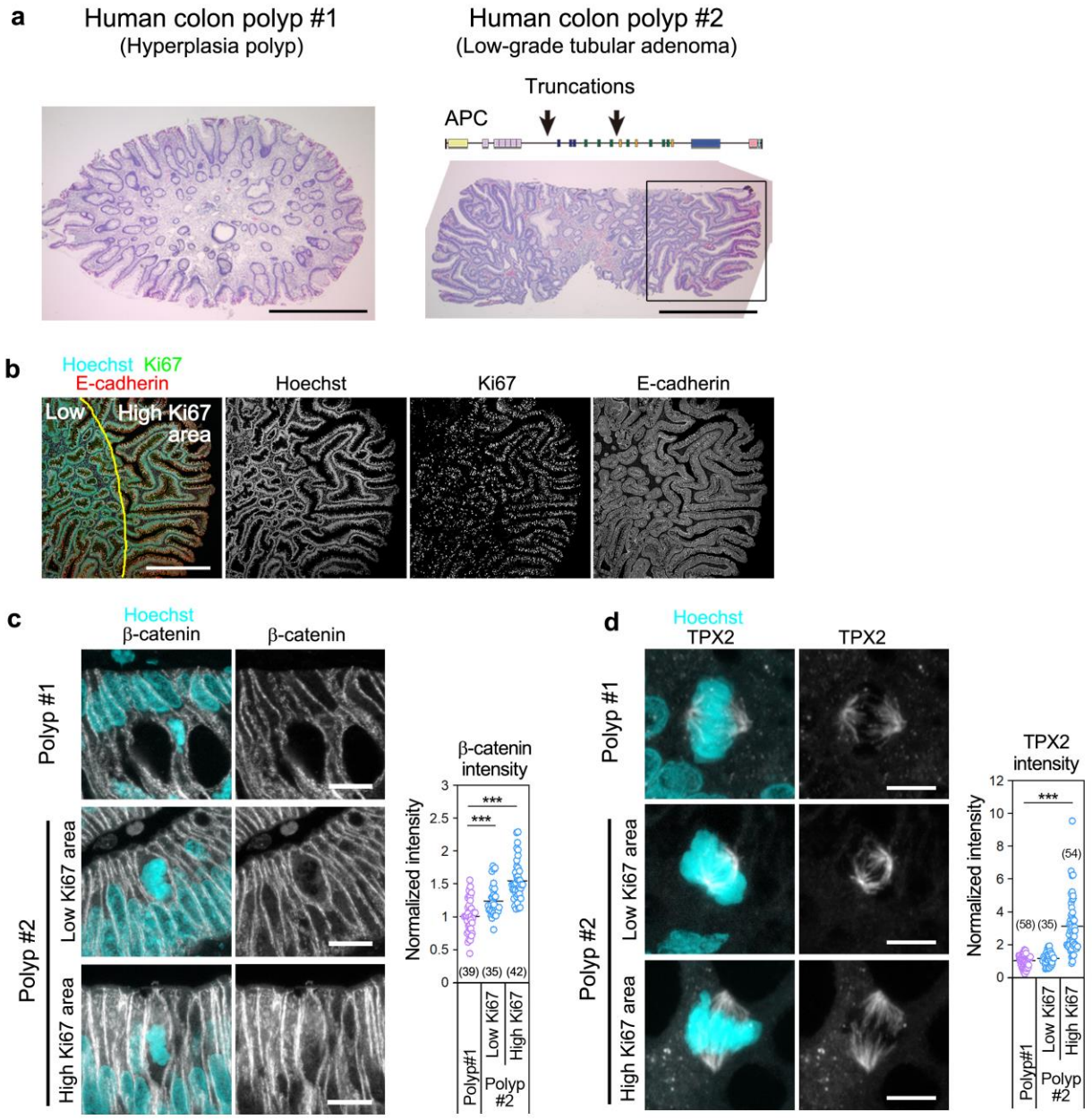

Extended Data Fig. 7 | Immunofluorescence analysis of paraffin-embedded sections of APC mutant human tumour tissues. (**a**) HE-stained sections of a human hyperplasia polyp without an APC mutation (polyp #1) (left) and a low-grade tubular adenoma with two APC truncation mutations (polyp #2) (right). Two mutant APC sequences detected in polyp #2 are shown

(arrows). For details, see Methods. (**b**) Ki67 proliferation index of the boxed area in (a) in polyp #2. Immunofluorescence staining of polyp #2 for E-cadherin and Ki67. Nuclear DNA was counterstained with Hoechst 33342. On the basis of the Ki67 intensity, the area was roughly divided into a highly proliferative region (outer, high Ki67 area) and moderately proliferative region (inner, low Ki67 area) as indicated by the yellow line. (**c**) Immunostaining of polyp #1 and #2 for β-catenin with nuclear DNA stained by Hoechst 33342. Representative images of the less proliferative area (low Ki67) and highly proliferative area (high Ki67) of polyp #2 are shown. Quantitative analysis of immunofluorescence signals of β-catenin in crypts and tumour tissues of nine polyps is shown on the right. Note that preferential accumulation of β-catenin in the nucleus was observed in all tumour tissues. (**d**) Immunofluorescence staining of polyp #1 and #2 for TPX2 with Hoechst 33342 counterstaining is shown. Examples of mitotic cells in the less proliferative area (low Ki67) and highly proliferative area (high Ki67) of polyp #2 are shown. Scale bars: 1 mm (a), 200 μm (b), 5 μm (c), 50 μm (d, left), and 20 μm (d, right). ***$P < 0.001$; Tukey–Kramer test.

Extended Data Figure 8 Kawasaki et al.

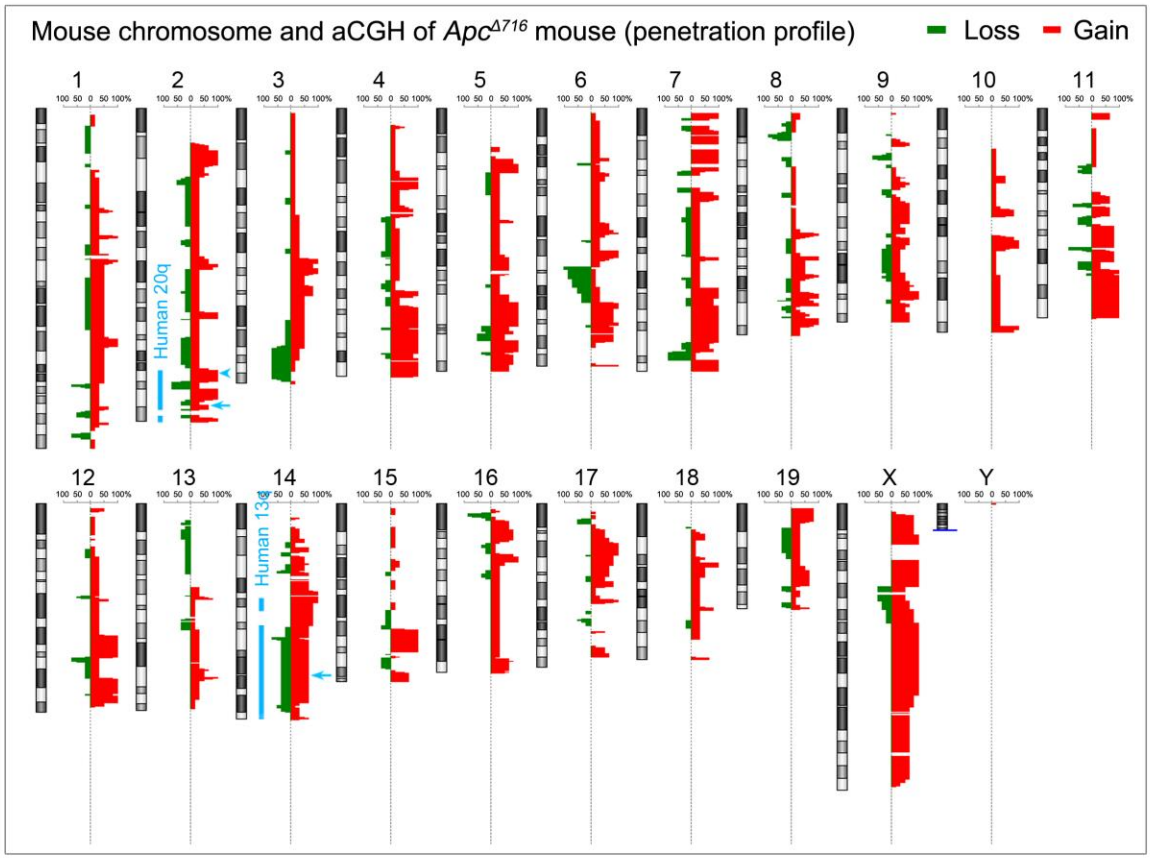

Extended Data Fig. 8 | aCGH analysis of mouse tumours. aCGH analysis of chromosomes in three independent *Apc*$^{\Delta 716}$ mouse polyps. A penetration profile of copy number changes from duplicate analysis is shown. Syntenic regions of human chromosome 20q and 13q on mouse chromosomes are indicated by cyan lines. Arrow and arrowhead on chromosome 2 indicate the loci of *Aurka* and *Tpx2*, respectively. Arrow on chromosome 14 indicates the locus of *Bora*.

References

1. Aoki K, Taketo MM. Adenomatous polyposis coli (APC): a multi-functional tumor suppressor gene. *J Cell Sci* **120**, 3327-3335 (2007).
2. Fearnhead NS, Britton MP, Bodmer WF. The ABC of APC. *Human molecular genetics* **10**, 721-733 (2001).
3. Polakis P. The adenomatous polyposis coli (APC) tumor suppressor. *Biochimica et biophysica acta* **1332**, F127-147 (1997).
4. Fodde R, Smits R. Disease model: familial adenomatous polyposis. *Trends in molecular medicine* **7**, 369-373 (2001).
5. Pronobis MI, Rusan NM, Peifer M. A novel GSK3-regulated APC:Axin interaction regulates Wnt signaling by driving a catalytic cycle of efficient betacatenin destruction. *eLife* **4**, e08022 (2015).
6. Näthke IS. The adenomatous polyposis coli protein: the Achilles heel of the gut epithelium. *Annual review of cell and developmental biology* **20**, 337-366 (2004).
7. Banks JD, Heald R. Adenomatous polyposis coli associates with the microtubule-destabilizing protein XMCAK. *Current biology : CB* **14**, 2033-2038 (2004).
8. Powell SM, *et al.* APC mutations occur early during colorectal tumorigenesis. *Nature* **359**, 235-237 (1992).
9. Horii A, *et al.* The APC gene, responsible for familial adenomatous polyposis, is mutated in human gastric cancer. *Cancer research* **52**, 3231-3233 (1992).
10. Boynton RF, *et al.* Loss of heterozygosity involving the APC and MCC genetic loci occurs in the majority of human esophageal cancers. *Proceedings of the National Academy of Sciences of the United States of America* **89**, 3385-3388 (1992).

11. Nishisho I, *et al.* Mutations of chromosome 5q21 genes in FAP and colorectal cancer patients. *Science* **253**, 665-669 (1991).

12. Kinzler KW, *et al.* Identification of a gene located at chromosome 5q21 that is mutated in colorectal cancers. *Science* **251**, 1366-1370 (1991).

13. Joslyn G, *et al.* Identification of deletion mutations and three new genes at the familial polyposis locus. *Cell* **66**, 601-613 (1991).

14. Groden J, *et al.* Identification and characterization of the familial adenomatous polyposis coli gene. *Cell* **66**, 589-600 (1991).

15. Miyoshi Y, *et al.* Somatic mutations of the APC gene in colorectal tumors: mutation cluster region in the APC gene. *Human molecular genetics* **1**, 229-233 (1992).

16. Oshima M, Oshima H, Kitagawa K, Kobayashi M, Itakura C, Taketo M. Loss of Apc heterozygosity and abnormal tissue building in nascent intestinal polyps in mice carrying a truncated Apc gene. *Proceedings of the National Academy of Sciences of the United States of America* **92**, 4482-4486 (1995).

17. Su LK, *et al.* Multiple intestinal neoplasia caused by a mutation in the murine homolog of the APC gene. *Science* **256**, 668-670 (1992).

18. Moser AR, Pitot HC, Dove WF. A dominant mutation that predisposes to multiple intestinal neoplasia in the mouse. *Science* **247**, 322-324 (1990).

19. Smits R, *et al.* Apc1638T: a mouse model delineating critical domains of the adenomatous polyposis coli protein involved in tumorigenesis and development. *Genes & development* **13**, 1309-1321 (1999).

20. Fodde R, *et al.* Mutations in the APC tumour suppressor gene cause chromosomal instability. *Nature cell biology* **3**, 433-438 (2001).

21. Chen BC, *et al.* Lattice light-sheet microscopy: imaging molecules to embryos at high spatiotemporal resolution. *Science* **346**, 1257998 (2014).

22. Widlund PO, *et al.* XMAP215 polymerase activity is built by combining multiple tubulin-binding TOG domains and a basic lattice-binding region. *Proceedings of the National Academy of Sciences of the United States of America* **108**, 2741-2746 (2011).

23. Xia Z, *et al.* AURKA governs self-renewal capacity in glioma-initiating cells via stabilization/activation of beta-catenin/Wnt signaling. *Molecular cancer research : MCR* **11**, 1101-1111 (2013).

24. Soule HD, *et al.* Isolation and characterization of a spontaneously immortalized human breast epithelial cell line, MCF-10. *Cancer research* **50**, 6075-6086 (1990).

25. Cowell JK, LaDuca J, Rossi MR, Burkhardt T, Nowak NJ, Matsui S. Molecular characterization of the t(3;9) associated with immortalization in the MCF10A cell line. *Cancer genetics and cytogenetics* **163**, 23-29 (2005).